Additive manufacturing of refractory multi-principal element alloy with ultrahigh-temperature strength via simultaneous enhancements in printability and solid solution hardening

Ran Duan [a)], Yakai Zhao [c)], Jintao Xu [a)], Qingjun Zhou [d)], Zhenyu Yan [d)], Yong Xie [d)], Peng Dong [d)], Kai Feng [a,b)*], Zhuguo Li [a,b) **], Beibei Xu [g)***], Xiubing Liang [e)], Upadrasta Ramamurty [c,f)]

[a)] Shanghai Key Laboratory of Materials Laser Processing and Modification, School of Materials Science and Engineering, Shanghai Jiao Tong University, Shanghai, 200240, China

[b)] Collaborative Innovation Center for Advanced Ship and Deep-Sea Exploration, Shanghai, 200240, China

[c)] Institute of Materials Research and Engineering (IMRE), Agency for Science, Technology and Research (A*STAR), Singapore, 138634, Republic of Singapore

[d)] Capital Aerospace Machinery Co., Ltd., Beijing, 100076, China

[e)] National Institute of Defense Technology Innovation, Academy of Military Sciences PLA China, Beijing, 100076, China

[f)] School of Mechanical and Aerospace Engineering, Nanyang Technological University, Singapore, 639798, Republic of Singapore

[g)] State Key Laboratory of Materials for Integrated Circuits, Shanghai Institute of Microsystem and Information Technology, Shanghai, 200050, China

*Corresponding Author:

E-mail address: fengkai@sjtu.edu.cn (Kai Feng).

E-mail address: lizg@sjtu.edu.cn (Zhuguo Li).

E-mail address: xubb@mail.sim.ac.cn (Beibei Xu).

Highlights

- Utilization of the parameters for solid solution hardening and printability parameters to identify the alloy composition that results in high temperature strength and is amenable to LPBF.
- Printability was enhanced to a density of 99.2% by prioritizing low liquid viscosity, wide liquid temperature range, and minimizing thermal deformation.
- Composition optimization effectively increased the sub-boundary proportion and refined the grain size to 6.1 ± 1.2 μm.
- $Nb_{15}Ta_{10}W_{75}$ RMPEAs exhibited excellent room temperature strength of 1409 MPa and ultra-temperature strength of 640 MPa at 1600 ℃.

Abstract

Refractory multi-principal element alloys (RMPEAs), such as those obtained from the Nb-Mo-Ta-W system, are known for remarkable high-temperature strength. However, their brittleness poses a significant challenge in manufacturing engineering components through conventional methods. Alloying with other elements, while mitigating this problem, can compromise the high temperature strength. To this end, a composition optimization strategy within the Nb-Mo-Ta-W alloy system was developed to simultaneously enhance ultrahigh-temperature strength through solid solution hardening (SSH) and printability (through the use of the thermodynamic criteria) for laser powder bed fusion (LPBF). The thermodynamic parameters that enhance printability are lower liquid viscosity (*LV*) and higher liquid temperature range (*LR*) for better liquidity in filling pores, lower volumetric change (*VC*) that minimizes cracking susceptibility, and lower shear to bulk moduli ratio (μ/B) that improves toughness. Analysis shows that a higher $LR/VC*LV*(\mu/B)$ leads to better printability. An optimum alloy composition ($Nb_{15}Ta_{10}W_{75}$) that balances strength and printability was obtained by considering SSH and the thermodynamic criterion and experimentally validated. The effects of chemical composition optimization on printability, microstructure, and temperature-dependent strength were analyzed through thermodynamic calculations, microstructure characterization, and strengthening contribution estimations.

Keywords: *Composition optimization; Refractory multi principal element alloys; Laser powder bed fusion; Solid Solution Hardening; Printability; Ultrahigh-temperature strength.*

1. Introduction

An ever-growing demand for materials with ultrahigh-temperature strength exists [1] and refractory multi-principal element alloys (RMPEAs) are promising candidates for it [2-5]. For instance, the strength of NbMoTaW RMPEAs (405 MPa) at 1600 ℃ surpasses those of the Ni-based superalloys [6]. However, their brittleness is a major challenge, particularly for obtaining components with intricate designs and complex shapes. Utilizing laser powder bed fusion (LPBF) would allow for the direct fabrication of such structural components, and, in the process, overcome the limitations of traditional sintering molds [7-9]. Therefore, it would be of interest to identify the suitable compositions within the Nb-Mo-Ta-W family of RMPEAs that are amenable to LPBF, whereas the main focus, hitherto, has been on enhancing their strength through the introduction of metallic or non-metallic alloying elements during the casting processes. For example, Han et al. [10] developed NbMoTaWTi RMPEAs with compressive yield strengths of 1343 MPa at room temperature (RT, ~25 °C) and 620 MPa at 1000 ℃. Li et al. [11] successfully synthesized NbMoTaWZr RMPEAs with strengths of 1607 MPa at RT and 555 MPa at 1000 ℃. Tong et al. [12] fabricated NbMoTaWHf RMPEAs with a strength of 1252 MPa at RT. The enhanced strength reported in these studies is attributed to the increased lattice distortion caused by the distinct atomic sizes of NbMoTaW RMPEAs and Ti, Zr, and Hf elements [12,13]. Nevertheless, using elemental powders with distinct thermodynamic properties for printing experiments is prone to generate defects, as there are considerable disparities between high-melting point elements such as Nb, Mo, Ta, and W, and relatively low-melting point elements such as Ti, Zr, and Hf, in terms of their thermodynamic characteristics such as melting point, viscosity, thermal expansion [14]. Such differences could significantly and adversely impact the melt flow and material deformation behavior during LPBF [15-19]. As a consequence, the printing process window is likely to become narrower and/or the fabricated samples could contain large volume of defects such as pores and cracks [18-21]. Therefore, designing Nb-Mo-Ta-W RMPEAs that are amenable to LPBF and, simultaneously, have ultrahigh-temperature strength remains a significant challenge.

Incorporating additional alloying elements to NbMoTaW RMPEA is also a challenge for the aforementioned simultaneous optimization. The strength of NbMoTaW at 1600 ℃ is about 405 MPa, significantly higher than NbMoTaWX (X=Ti, Zr, Hf, or Cr) which is lower than 250 MPa at 1600 ℃ [22, 23]. This is because a higher

melting point delays the transition of dislocation slip from the cross-kinking mechanism to the diffusion-controlled one, thereby maintaining ultrahigh-temperature strength [24]. Besides, LPBF of Nb-Mo-Ta-W alloy system could become further complicated and difficult to control with the addition of new elements. Adding Ti or Ni powder to Nb, Mo, Ta elemental powder to print NbMoTaTi and NbMoTaNi samples, result in cracks and porosity caused by thermodynamic differences, as well as unmelted particles caused by differences in element melting points [15]. The "thermodynamic differences" refers to the different intrinsic properties of constituent elements, such as melting point, viscosity, and thermal expansivity [14, 25]. Therefore, adjusting the proportions of different elements in the Nb-Mo-Ta-W system without adding other elements offers a unique potential for simultaneously improving the strength and printability. It could enhance severe lattice distortion, which is beneficial for improving strength [26-30], and could also reduce thermodynamic differences between elements, which benefits the printability in general [18-21]. The minimal discrepancy between the elements of the Nb-Mo-Ta-W system, the more expedient it is to achieve the optimal printing parameters [18-21]. However, few studies focused on this aspect thus far.

Traditional trial-and-error methods are inadequate for quickly exploring high-temperature materials suitable for LPBF [31]. Keeping this in view, we adopted, in this study, a composition optimization strategy in the Nb-Mo-Ta-W RMPEA system that adjusts the element contents to improve the high-temperature strength and printability simultaneously. The extent of SSH, a significant contributor to the high-temperature strength, was evaluated by using the Toda-Caraballo model based on the local lattice variation, which has the ability to overcome the compositional complexity [32]. Printability evaluation relied on thermodynamic parameters such as liquid viscosity, liquid temperature range, and volume change, reflecting physical transformation characteristics during LPBF. A multiplication plot of high-temperature strength and printability was then drawn in order to pin-point the optimal composition. A novel $Nb_{15}Ta_{10}W_{75}$ RMPEAs with ultrahigh-temperature strength and excellent printability was designed through this strategy. We also printed NbMoTaW RMPEAs to compare the optimization effect. $Nb_{15}Ta_{10}W_{75}$ has a higher density of 99.2 % and finer average grain size of 6.1 ± 1.2 μm compared to NbMoTaW RMPEAs with density of 97.6 % and average grain size of 10.1 ± 1.4 μm. Strength was improved to 1409 MPa at RT, while high-temperature strength was significantly improved to 640 MPa at 1600 ℃. The

effects of composition optimization on the printability, microstructure characteristics, and temperature-dependent strength are discussed.

2. Materials and methods

2.1. Material design

Amongst various refractory elements of interest, Nb, Mo, Ta, and W have the highest melting points [13]. Hence, they were selected in this work for the design of RMPEAs possessing good high-temperature properties. In general, SSH plays a vital role in enhancing the strength of alloys [33, 34]. Using the experimental results obtained on single principal component alloys for fitting and extrapolation of the SSH values can be reasonably accurate. For instance, Choi et al. [35] have made significant progress in pursuing accurate evaluation of the SSH effects by analyzing the orientation dependency of solid solution hardening in TWIP steel, which is beneficial for accurately evaluating the contribution of elements in enhancing SSH. However, the experimental results reported on the Nb-Mo-Ta-W RMPEAs are sparse, which limits the precise evaluation of SSH in this system at present. While grain orientation plays an important role in SSH, incorporating it into SSH analysis would necessitate extensive experiments and data. This is because the orientation dependence of SSH involves intricate crystallographic analysis that requires careful experiments to obtain the quantitative relationship between crystallographic orientation and SSH in the Nb-Mo-Ta-W system, as detailed in the Supplementary Note 1. In addition, traditional approaches that assess the efficacy of SSH rely on the "solute-solvent" concept in binary alloys [36]. It is challenging to distinguish solute and solvent in RMPEA, which brings about difficulty in directly applying conventional SSH theories to them. Given the challenges associated with the experiments and shortcomings in theoretical concepts, the Toda-Carabello model was selected in the present study to provide a better understanding and approximate estimate of the SSH in the Nb-Mo-Ta-W system.

The Toda-Caraballo model uses a matrix to describe the lattice distortion arising from different elements [32]. This model enables an efficient assessment of the strength of the SSH for RMPEAs. The principle employed is that each element sequentially acts as a solute, while other remaining elements act as solvents until all elements are alternated, which is used for estimating the degree of local lattice distortion. Solid solution strength is calculated based on the lattice distortion caused by the fluctuations

in the composition, rather than the solute-solvent interaction. This model can more comprehensively calculate the influence of each element in RMPEAs on strength. Moreover, using the Toda-Caraballo model to evaluate SSH that could occur during the LPBF process is consistent with the atomic diffusion characteristics inherent to it. The rapid cooling rates and the small melt pool dimensions associated with the LPBF process impede the rapid diffusion of solute and solvent atoms, limiting the generation of concentration gradients over a large range (micrometer level). The Toda-Caraballo model considers the effect of solvent-solute interactions on lattice distortion by introducing a minimal component fluctuation, without considering concentration gradients over a large range. This model could be expressed as [32, 37]:

$$\Delta\sigma_{SSH} = 6Z\mu\left(\frac{\xi\phi}{a}\right)^{4/3} X \left|D\right|^{4/3} X' \tag{1}$$

$$D = \begin{pmatrix} 0 & \frac{da}{x_1^2} & \cdots & \frac{da}{x_1^n} \\ \frac{da}{x_2^1} & 0 & \cdots & \frac{da}{x_2^n} \\ \vdots & \cdots & \ddots & \vdots \\ \frac{da}{x_n^1} & \frac{da}{x_n^2} & \cdots & 0 \end{pmatrix} \tag{2}$$

$$\mu = \sum_{i}^{n} x_i \mu_i \tag{3}$$

$$\frac{da}{x_i^j} = (XSX' - X_i^j SX'^j_i)\ \frac{1}{\delta x} \tag{4}$$

$$X = (x_1, x_2, ..., x_n) \tag{5}$$

$$X_1^n = (x_1 - \delta x, x_2, ..., x_n + \delta x) \tag{6}$$

$$S_{lat} = \sum_{i}^{n}\sum_{j}^{n} s_{ij} x_i x_j \tag{7}$$

$$S_{lat} = af \tag{8}$$

$$s_{ij} = \frac{s_{ii}^2 B_{ii} x_i + s_{jj}^2 B_{jj} x_j}{s_{ii} B_{ii} x_i + s_{jj} B_{jj} x_j} \tag{9}$$

where Z is a fitting constant (optimized to be 55) [32], μ is the shear modulus, ξ is a constant (= 2 [32]), ϕ represents the interaction forces (determined as 16) [38], a is the lattice parameter [32], D is the variation in the lattice parameter [32], da/x_{ij} represents the variation in the lattice parameter when replacing an atom of element i with element j [32], X_{1n} denotes the minimal lattice parameter variation, δ_x represents an infinitesimally small concentration variation [32], X' represents the transposed operation of the matrix, XDX' means the variation of lattice parameters with changes in composition, x_i is the solute content of i, S_{lat} is the average interatomic spacing [37], $S=\{s_{ij}\}$ is a matrix for interatomic spacing, f is an atomic packing factor (=$1/\sqrt{2}$ for BCC) [38], s_{ii} and s_{jj} denote

the nearest neighbor distances for elements *i* and *j*, and B_{ii} and B_{jj} represent the bulk modulus of elements *i* and *j*, respectively.

For illustrating the compositional dependence of SSH in the Nb-Mo-Ta-W system, the strength distribution maps shown in Fig. 1 were created using the Toda-Caraballo model. The value of x in SSH distribution maps increases from 0 to 25%. This is because equiatomic ratio has the highest degree of lattice distortion [39]. From Fig. 1, it can be observed that SSH gradually increases with the number of elements. Notably, the red component range (as marked out by red circle) in $NbMo_xTaW$ RMPEAs overall exhibits more significant SSH than the other three RMPEA systems with varying Ta, Nb, or W contents, and is comparable to the quaternary Nb-Mo-Ta-W RMPEAs (> 300 MPa).

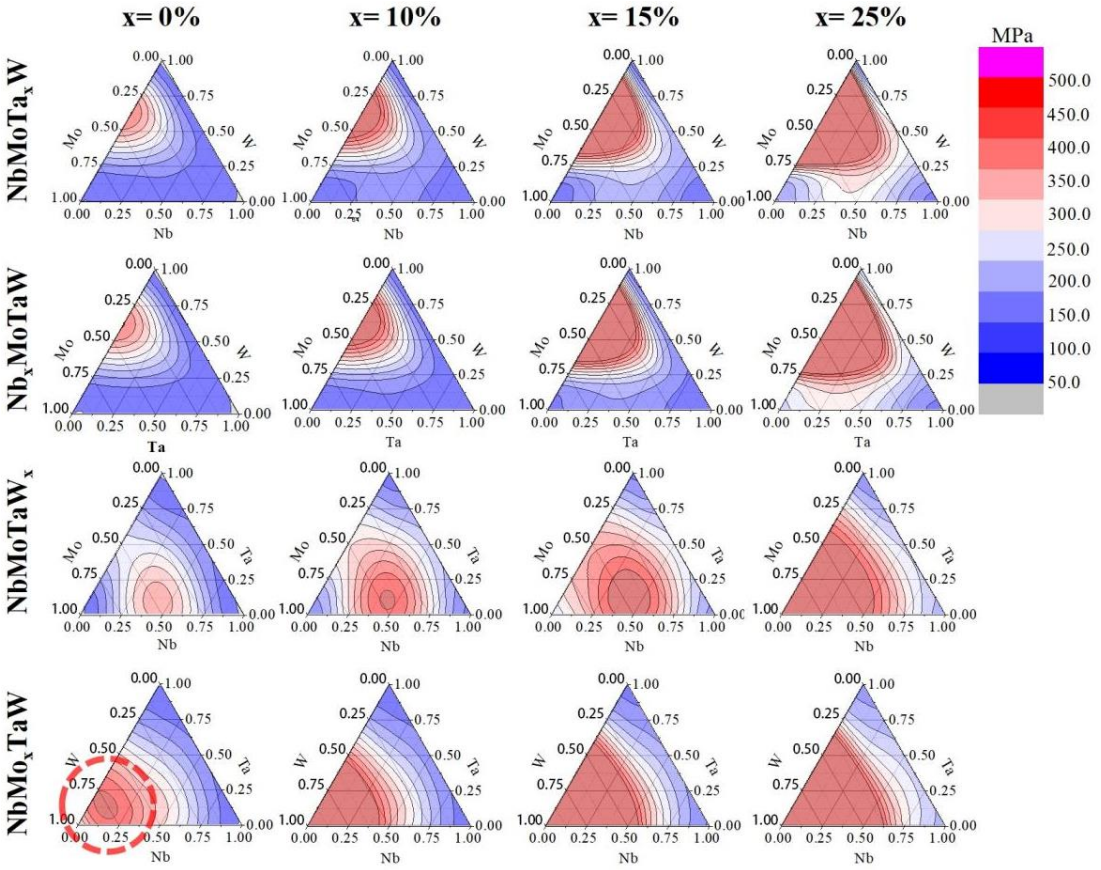

Fig. 1. Solid solution hardening distribution maps of the Nb-Mo-Ta-W RMPEA system.

The LPBF process involves multiphysics (of powder flow, laser-material interaction, melting and solidification of the alloy, fluid mechanics of the molten metal, heat transfer through convection, conduction and radiation mechanisms, and so on) and

hence is considerably complex to model. The physical transformation characteristics of the alloy can be captured through the thermodynamic parameters [15-19]. At the initial stages of LPBF, the powder melts into a liquid. The liquid flow characteristics can be described by the melt liquid temperature range (LR) and the liquid viscosity (LV) [16, 18]. In the subsequent solidification process, solidified layers undergo rapid thermal cycling deformation, which results in thermal stress accumulation and cracking tendency. The degree of thermal deformation can be represented by the volumetric change (VC) that occurs due to solidification [16, 18]. Furthermore, the ductility or brittleness is broadly determined by the ratio of shear to bulk moduli (μ/B) according to the Pugh criterion ($\mu/B \leq 0.57$ for ductility and $\mu/B > 0.57$ for brittleness) [40]. This parameter quantifies the ability of the material to withstand thermal deformation. The Java-based Materials Properties (JMatPro) software was then used to calculate *LR*, *LV*, *VC*, μ, *B* of different compositions of interest at different temperatures [41, 42]:

$$P = \int \sum_i x_i P_i^0 + \sum_i \sum_{j>i} x_i x_j \sum_v \Omega_{ij}^v (x_i - x_j)^v \, dT/\Delta T \tag{10}$$

$$\omega = \frac{LR}{VC \times LV \times (\mu / B)} \tag{11}$$

where x_i is the molar fractions of the elements *i*, P_i^o is the thermophysical property of element *i* at temperature *T*, Ω_{ij}^v is an interaction parameter that is dependent on *v*, *v* is the order function, and parameter ω is a parameter that embodies the printability of the alloy (higher ω - better printability). During LPBF, the alloy experiences a wide temperature spectrum. Therefore, using the RT thermodynamic parameters to assess the printability would be erroneous. Keeping this in view, we utilized the integrated thermodynamic parameters at different temperatures for obtained analogous values (Eq. 10) to reflect the actual physical condition of LPBF. Based on the above thermodynamic estimations, our objective is to identify an alloy with an extensive *LR* and minimal *LV*, *VC*, and μ/B values to elevate printability.

The compositional dependence of ω in Nb-Mo-Ta-W RMPEAs is illustrated in Fig. 2. Obviously, nearly all the corner regions of triangles (except for corners containing Mo and Ta elements) show larger ω values than the center regions of triangle (multiple principal element content). Especially in the $NbMoTa_xW$ and $NbMo_xTaW$ alloys (x = 0%), the corner regions of high Nb or W contents (other elements content < 30%) all have the best printability (ω > 42× 10^2 ℃/mPa*s) amongst all, which are

marked by red circles. With the increasing x (= 10%, 15%, 25%), the regions where ω > 42 × 10^2 °C/mPa*s disappear, and continuously replaced by the expansion of regions with lower ω, reflecting a decrease in printability. Therefore, regions with high concentrations of Nb or W (other elements content < 30%) in NbMoTa$_x$W and NbMo$_x$TaW RMPEAs (x = 0%) show the best printability (>42×10^2 °C/mPa•s) amongst all.

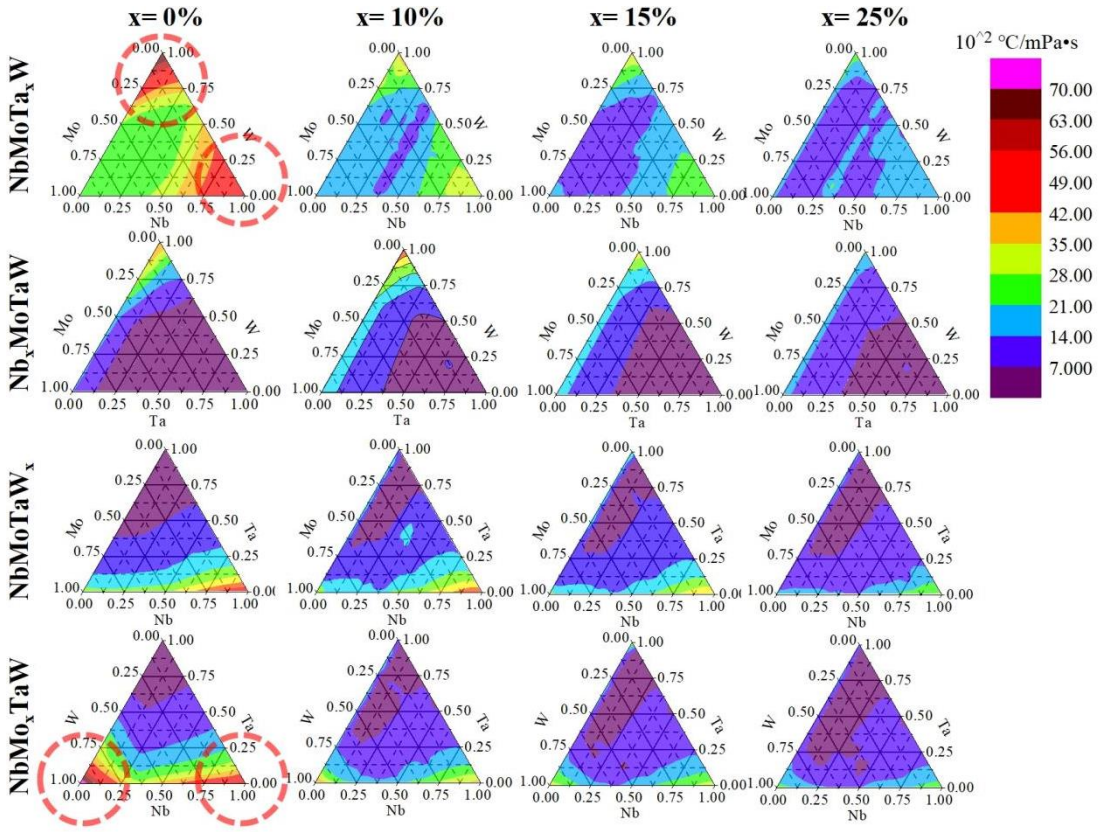

Fig. 2. Printability distribution maps of the Nb-Mo-Ta-W RMPEA system, developed based on the ω values representing the extent of SSH.

The equation given below, which transforms the different element contents into a unified measure, χ, is used to assess the impact of the chemical composition on printability and SSH of the alloy:

$$\chi = \sqrt{(x_{\mathrm{Nb}}^2 + x_{\mathrm{Mo}}^2 + x_{\mathrm{Ta}}^2 + x_{\mathrm{W}}^2)} \tag{12}$$

where x_{Nb}, x_{Mo}, x_{Ta}, and x_{W} are the contents of different elements (in at%.). A higher χ value corresponds to the higher content of a single element. Utilizing the data from Figs.

1 and 2, the changes in the printability and SSH with χ are plotted in Fig. 3(a). It is observed that with an increase in χ (i.e., decrease in different elements contents), the overall SSH showed a downward trend, whereas the printability increases.

To identify the optimal balance between SSH and printability, $\boldsymbol{\omega}$ and $\boldsymbol{\Delta\sigma_{SSH}}$ were multiped for different compositions. This is because $\boldsymbol{\omega}$ and $\boldsymbol{\Delta\sigma_{SSH}}$ move in opposite directions with the variation in the alloy composition (Fig. 3(a)). It was envisioned that a simple multiplication of them can lead to the identification of the maximum value under mutual constraint. Fig. 3(b) shows the maximum values between $\boldsymbol{\omega}$ and $\boldsymbol{\Delta\sigma_{SSH}}$ within each 1% interval of χ. It was observed that numerical points follow a certain pattern, thus the following polynomial function was used for curve fitting:

$$\sigma\omega = 2223 + 29 \times (9.2/(4 \times (\chi - 77.9)^2 + 85)). \quad (13)$$

A peak in the fitted curve is noted (at χ = 75–83%), with $\boldsymbol{\sigma\omega}$ increasing first and then decreasing. The initial increase in is due to the fact that $\boldsymbol{\sigma\omega}$ will increase with χ (Fig. 3(a)) until it reaches the maximum value. The peak corresponds to the $NbMo_xTaW$ (x=0%) system, and hence the optimal composition was determined as $Nb_{15}Ta_{10}W_{75}$ which should have the best balance between high temperature strength and printability.

In Table 1, the key values of SSH and thermodynamic parameters of $Nb_{15}Ta_{10}W_{75}$ and NbMoTaW RMPEAs were compared to elucidate the possible reasons for the improved strength and printability. The influence of the SSH mechanism on strength resulted from the variations in *XDX'*, μ, and *B*, as determined by Eq. (1). Local compositional variations, caused by the lattice distortion, impede dislocation glide and enhance strength, which is reflected by *XDX'* [32]. While μ signifies resistance to shear deformation, *B* represents incompressibility and ductility [37]. $Nb_{15}Ta_{10}W_{75}$ RMPEA has higher μ and *B* and lower *XDX'*, compared to NbMoTaW, with similar SSH. The printability was evaluated based on *LR*, *LV*, *VC*, and μ/B, using Eq. (11). Higher *LV* and lower *LR* represent smoother and uninterrupted flow of the molten metal, which could better fill any microcracks that form during the solidification process [25]. Specifically, higher *LV* and lower *LR* can provide more and smoother liquid at grain boundaries during LPBF solidification, thereby avoiding the risk of grain boundary rupture caused by lack of molten liquid during solidification shrinkage, and thus reducing defects [43]. A lower *VC* corresponds to less volume shrinkage and hence lower cracking tendency [25]. The parameter μ/B was utilized to assess the toughness of the matrix [25]. The

$Nb_{15}Ta_{10}W_{75}$ RMPEA exhibited a higher *LR* and lower *VC* than the NbMoTaW RMPEAs. Since the other thermodynamic parameters are similar, it should have better printability.

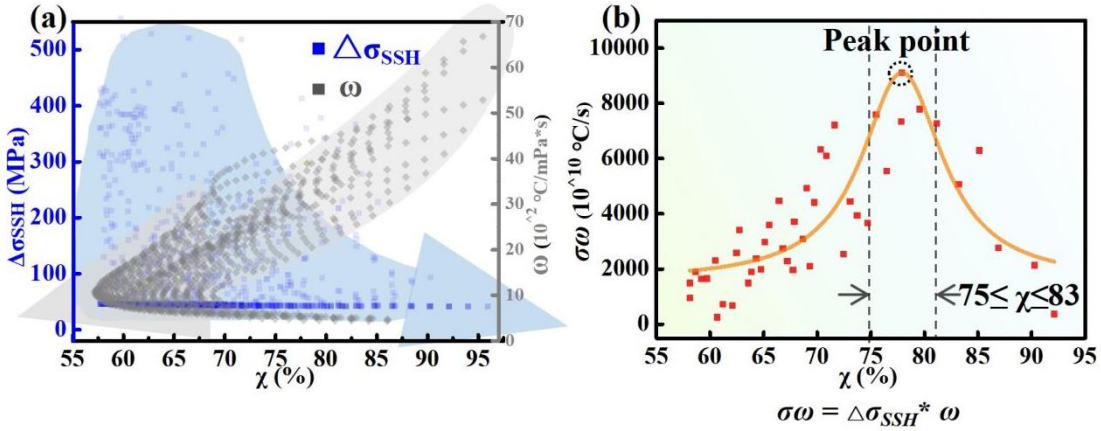

Fig. 3. Variation of printability and SSH parameters with different element contents in the Nb-Mo-Ta-W RMPEA system. (a) Maximum multiplication values between printability and SSH effect to find the optimal equilibrium (b).

Table 1. Key values of the SSH and thermodynamic properties.

	SSH effect					Printability			
	XDX' **(%)**	***μ*** **(GPa)**	***B*** **(GPa)**	**$\triangle\sigma_{SSH}$ (MPa)**	***LR*** **(℃)**	***LV*** **(mPa•s)**	***VC*** **(%)**	***μ*/B**	***ω*** **($10^{\wedge 2}$℃/mPa•s)**
NbMoTaW	3.1	98	241	354	1130	9.5	40.1	0.40	7.4
$Nb_{15}Ta_{10}W_{75}$	2.6	108	278	337	1350	9.8	14.2	0.38	26.0

2.2. Material fabrication

Powders of Nb, Mo, Ta, and W that are 99.9 % pure, with the particle size ranging from 15 to 53 μm, were utilized for LPBF. An electronic analytical balance was used to accurately weigh the powders required for the composition of NbMoTaW and $Nb_{15}Ta_{10}W_{75}$ RMPEA. The pre-mixed powders were mechanically mixed in a planetary mill for 8 hours to ensure homogeneity. The powder mixtures were kept at 120 ℃ for 8 hours in a vacuum oven to eliminate moisture and improve the powder fluidity. The laser absorptivity and reflectivity of them were analyzed by using a UV-Vis spectrometer (Lamda 950, PerkinElmer, Inc.). An iSLM 280 three-dimensional (3D) metal printer equipped with 500 W Nd: YAG fiber laser (Zhong Rui Technique, China) was used for LPBF. Argon gas was utilized as the atmosphere with oxygen content < 100 ppm, minimizing oxidation during fabrication. The melting points of Nb, Mo, Ta,

and W all exceed 2500 ℃, necessitating a significant high-energy input for powder melting. The optimal process parameter combination (arrived at after a process parameter optimization work done *a priori*) is as following: Laser power (*P*) at 300 W, scanning speed (*V*) at 400 mm/s, layer thickness (*d*) at 40 μm, and hatch spacing (*h*) at 30 μm. Cubic samples (6 mm × 6 mm × 8 mm) were fabricated for microstructural analysis, and cylindrical specimens (Φ2 mm × 4 mm) were used for compression testing. A commercially available software package, JMatPro, was used to calculate phase diagrams and thermodynamic properties.

2.3. Microstructural characterization

Mesoscopic defects formed during LPBF were characterized using optical microscopy (OM; Axio Imager A2m, Zeiss, Germany). The density of the fabricated samples was measured by using a gas expansion density tester (HX-TD, Hiseel, China). A Quanta 200 FEG scanning electron microscope (SEM; FEI Co., USA) equipped with energy dispersive spectroscopy (EDS) and electron backscatter diffraction (EBSD) detectors was used to analyze the chemical composition and microstructure. The scanning area for EBSD was 120 μm × 120 μm (in each case) with a step size of 0.5 μm. The crystal structures of the microstructural phases were analyzed using an X-ray diffractometer (XRD; D8 ADVANCE Da Vinci, Bruker Corp., USA) with the Cu Kα radiation. A transmission electron microscope (TEM; JEM-F200X, JEOL Ltd., Tokyo, Japan) was used to further confirm the phase structure and lattice constant, with a working voltage of 200 kV. TEM samples were firstly mechanical thinned down to 20–40 μm, and then electropolished in 10% perchloric acid solution using a twin-jet electrochemical polisher at 40 V. Three-dimensional atom probe tomography (3D-APT; LEAP 5000X) was used to characterize the elemental distribution at grain boundaries with a pulse repetition rate of 200 kHz and a UV laser energy of 60 pJ. The tip-shaped specimens for 3D-APT were obtained through annular milling around grain boundaries, which was fabricated by a focused ion beam (FIB; Carl Zeiss AG) equipped with an electron beam at 100 kV.

2.4. Mechanical characterization

Room-temperature uniaxial compression tests were performed using a SANS CMT5105 machine (Sans Testing Machine Co., Ltd., Shenzhen, China) equipped with

a video extensometer (LVE-MICRO30) at a loading rate of 0.008 mm/s. The size of RT compression specimens was Φ 2 mm × 4 mm. At least three samples were tested for each condition. The high-temperature compression tests were performed using a Gleeble-3500 testing machine. The samples were heated to the desired testing temperatures at a rate of 10 ℃/min, held for 15 min, and then subjected to compression. The size of high temperature compression specimens was Φ 4 mm × 8 mm, with a constant strain rate of 0.0025 mm/s.

3. Results

3.1. Microstructural characterization

The morphology and size distribution of the powders used for LPBF are shown in Figs. 4(a) and (b). The measured sphericities of Nb, Mo, Ta, and W powders are 91 ± 0.1%, 93 ± 0.15%, 95 ± 0.18%, and 89 ± 0.5% respectively, which indicate good sphericity. The powder particle size distributions are in the range of 20–70 μm for Nb, 15–61 μm for Mo, 27–70 μm for Ta, and 17–55 μm for W. Figs. 4(c) and 4(d) display the reflectance and absorption of the elemental powders and the mixed powders. The absorption factor was compared at a wavelength of 1065 nm, same as that of the Nd: YAG fiber laser used for LPBF. Laser absorption rates of Nb, Mo, Ta, and W were measured to be 56%, 54%, 37%, and 64%, respectively. After powder mixing, the reflectivity values of NbMoTaW and $Nb_{15}Ta_{10}W_{75}$ powder were 65% and 62%, and the absorption was 53% and 56%, respectively. The high content of W in the $Nb_{15}Ta_{10}W_{75}$ powder improves the laser absorption compared to that in NbMoTaW powder. The high laser absorption rate of $Nb_{15}Ta_{10}W_{75}$ can be attributed to the following reasons. Firstly, the higher W content which has excellent laser absorption capacity improves the overall laser absorptivity of the $Nb_{15}Ta_{10}W_{75}$ powders. This is because W has a unique electronic structure with a partially filled d-orbital ($5d^4$), which makes its outermost electrons more unstable and easier to absorb energy than Nb, Mo, Ta . Secondly, W powder has a smaller size than Nb, Mo, Ta (Fig. 4(b)), so the larger quantity of W powder contained in $Nb_{15}Ta_{10}W_{75}$ provides a larger specific surface area for interaction with lasers, thereby improving the laser absorptivity. Improving the powder laser absorption was beneficial for increasing the energy input and LPBF with relatively lower power.

Fig. 4(e) shows the XRD patterns obtained on the LPBF $Nb_{15}Ta_{10}W_{75}$ and NbMoTaW. Indexing of the diffraction peaks shows that both the alloys contain only a single phase with the body-centered cubic (BCC) crystal structure, with no additional diffraction peaks associated with any other phases. Based on the XRD data, the lattice parameters of $Nb_{15}Ta_{10}W_{75}$ and NbMoTaW RMPEAs are estimated as 3.08 Å and 3.06 Å, respectively. Interestingly, XRD performed on the plane parallel to build direction (BD) found that the intensity of the $(211)_{BCC}$ peak is higher than the $(200)_{BCC}$ peak in both the NbMoTaW and $Nb_{15}Ta_{10}W_{75}$, indicating the presence of a certain degree of texture. Besides, the dislocation densities are estimated using the XRD results with the aid of the following equations [44, 45]:

$$\rho = \frac{2\sqrt{3}\varepsilon}{\psi b} \tag{14}$$

$$\varepsilon = \frac{\beta}{4\tan\theta} \tag{15}$$

$$\psi = \frac{K\lambda}{\beta\cos\theta} \tag{16}$$

$$\beta\cos\theta = \frac{K\lambda}{\psi} + (4\sin\theta)\varepsilon \tag{17}$$

where ρ is the dislocation density, ε is the micro-strain, ψ is coherent domain size, b is the Burgers vector magnitude, β is the full width at half maximum of the XRD peak, θ is the Bragg angle, K is a dimensionless factor of 0.89 [46, 47], and λ is the X-ray wavelength (0.154 nm here). ε is calculated using the Williamson Hall equation, which relates the half width of the XRD peak and the microstrain in the crystal [48]. ψ is obtained by using the Scherrer equation, which relates the half width of the XRD peak, X-ray wavelength, and the coherent domain size in the crystal [48]. The estimated dislocation densities in the LPBF $Nb_{15}Ta_{10}W_{75}$ and NbMoTaW samples are similar (3.45×10^{14} and 2.27×10^{14} m^{-2}, respectively).

Fig. 4(f) schematically illustrates the LPBF process. Building direction (BD) was aligned to the Z-axis. A scanning strategy of 67° rotation between successive layers was used. Cubic samples of NbMoTaW and $Nb_{15}Ta_{10}W_{75}$, each with a size of 10 × 10 × 5 mm^3, were manufactured, as shown in Fig. 4(g–h). The optimal densities of NbMoTaW and $Nb_{15}Ta_{10}W_{75}$ tested by gas expansion density tester were 97.6% and 99.2%, respectively. As $Nb_{15}Ta_{10}W_{75}$ shows better printability, it could be printed to larger samples (80 × 15 × 4 mm^3).

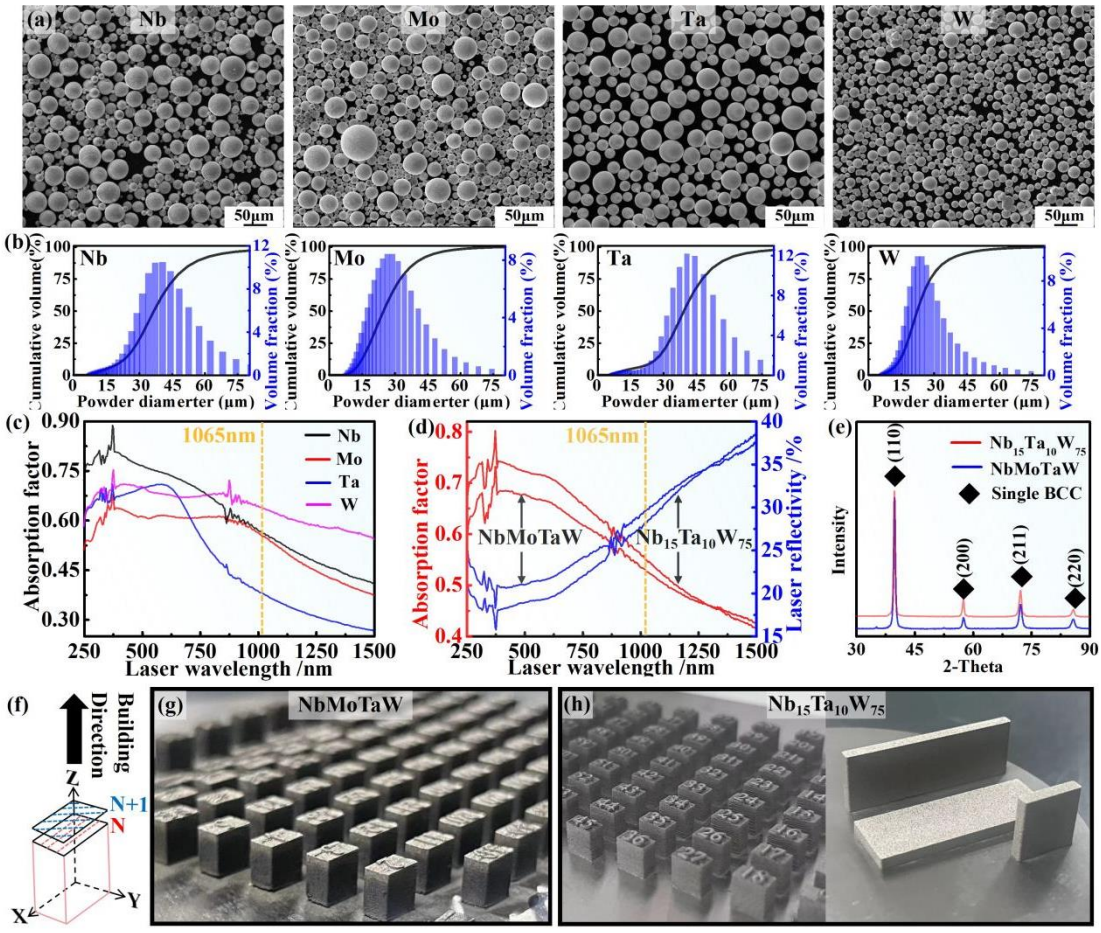

Fig. 4. Characterization of powder and printed samples: Particle morphology (a); Particle size distribution and equivalent diameter of the powders (b); Reflectance and absorption spectra of elemental powders and mixed powders (c-d); XRD scans of the LPBF samples (e); Schematic of scanning strategy used in LPBF process (f); Images of the as-printed specimens (g-h).

Figs. 5(a_1–a_4) show that the LPBF $Nb_{15}Ta_{10}W_{75}$ has an excellent density with minimal porosity, whereas NbMoTaW possesses larger porosity and microcracks (~10–25 μm in length). The corresponding EDS maps, Figs. 5(b_1–b_4), indicate to a homogeneous elemental distribution in both the alloys. The image quality (IQ) maps, showing the sub-grain and grain boundaries in the X-Y and X-Z sections for NbMoTaW and $Nb_{15}Ta_{10}W_{75}$, are displayed in Figs. 5(c1–c4). In general, the grain boundaries with misorientation angles ranging from 2° to 15° between the neighboring grains are considered as low angle grain boundaries (LAGBs), while those with angles exceeding 15° are classified as high angle grain boundaries (HAGBs) [49]. The inverse pole figure

(IPF) maps, showing the grain morphologies in the X-Y and X-Z sections for NbMoTaW and $Nb_{15}Ta_{10}W_{75}$, are shown in Figs. 5(d_1–d_4). The grains in the X-Z section display columnar morphology, whose long axes slightly deviate from BD (Z axis). This is because the grains tend to develop elongated columnar morphologies parallel to BD, driven by the most significant temperature gradient that occurs along it. However, the columnar grains cannot always align with BD due to frequent directional changes associated with the scanning strategy (Figs. 5(d_2) and (d_4)).

The geometrically necessary dislocation (GND) density maps are shown in Figs. 5(e_1–e_4). The number of kernels used to construct these maps are 433271, 421348, 526364, and 422364, respectively. It was observed that a large number of bright "blocky" areas are uniformly distributed in both NbMoTaW and $Nb_{15}Ta_{10}W_{75}$, implying that large number of dislocations were generated during LPBF. Besides, $Nb_{15}Ta_{10}W_{75}$ has a higher dislocation density on the X-Y and X-Z sections than NbMoTaW RMPEA. In the X-Y section, the dislocation density in NbMoTaW exceeds $1.2\times10^{14}/m^2$ in ~49.2% of the area examined, which increases to ~ 60.1% in $Nb_{15}Ta_{10}W_{75}$. In the X-Z section, the area fraction with dislocation density above $2.0\times10^{14}/m^2$ in NbMoTaW is ~30.9%, which increasessignificantly to ~43.3% in $Nb_{15}Ta_{10}W_{75}$. This result is close to the dislocation density values estimated using XRD and reflects the variation that the dislocation density in $Nb_{15}Ta_{10}W_{75}$ is higher than in NbMoTaW.

The deviation of columnar grain growth was confirmed through the pole figures (PFs) of the X-Y sections displayed in Figs. 5(f_1–f_4). The majority of the <001> orientations are concentrated within a circular region rather than concentrated in the center. In contrast, the cellular structure is reflected in the X-Y section. The fiber texture characteristics of the X-Y sections exhibit a weak crystallographic texture with maximum multiples of uniform distribution (MUD) values of 2.72 and 2.83, respectively. The distribution of grain orientation is generally random in the X-Y section.

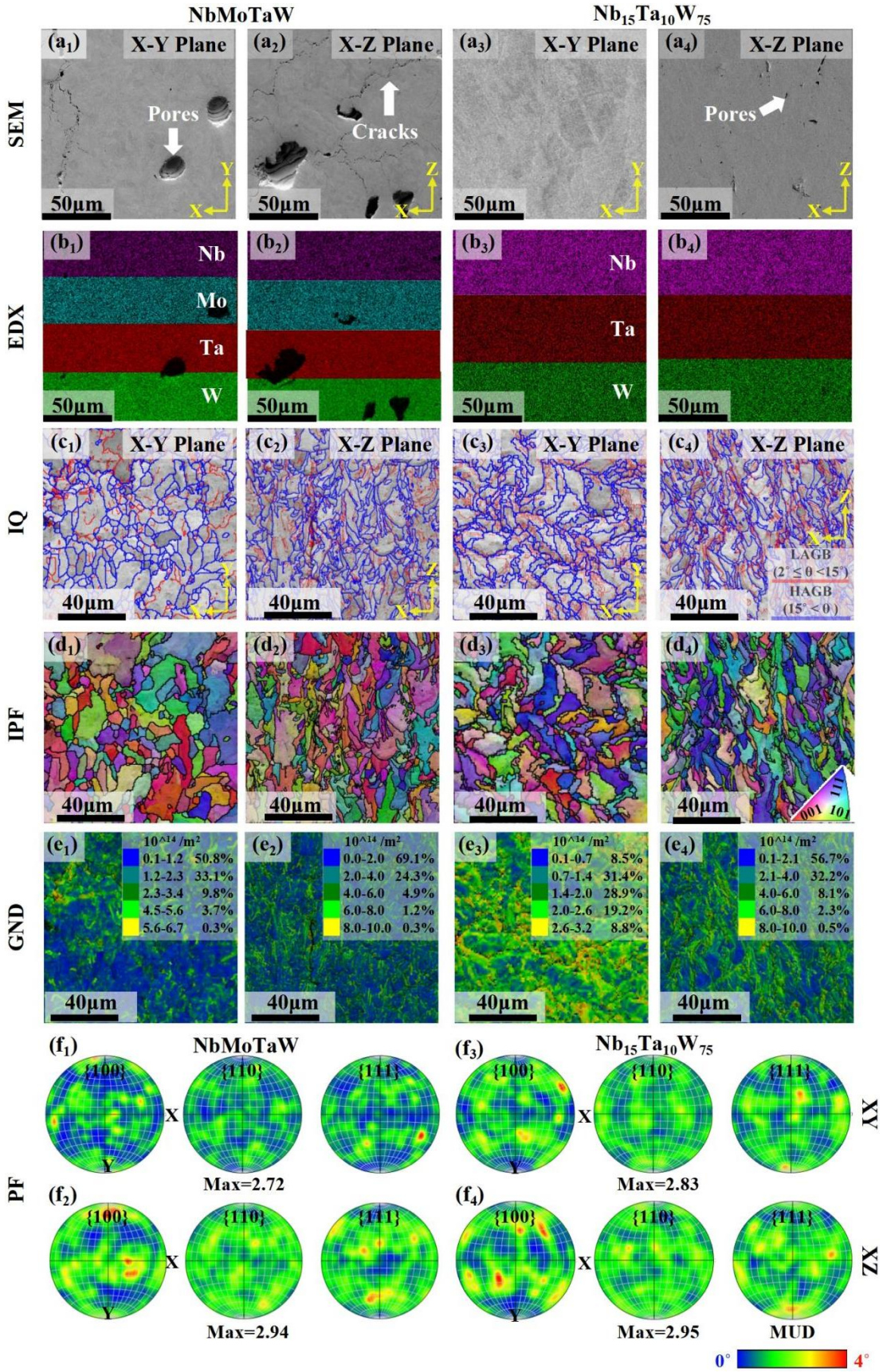

Fig. 5. Microstructural analysis of LPBF-fabricated NbMoTaW and $Nb_{15}Ta_{10}W_{75}$ RMPEAs: SEM revealing forming quality (a_1–a_4); EDS mapping revealing elements

uniformly distributed (b_1–b_4); Image quality maps revealing grain boundary distribution (c_1–c_4); Inverse pole maps reflecting grain morphology (d_1–d_4); GND images reflecting dislocation density distribution (e_1–e_4); Pole figures (f_1–f_4) corresponding to inverse pole maps (d_1–d_4);

Figs. 6(a_1–a_2) show the grain size distribution obtained from the statistical analysis of EBSD data. For NbMoTaW RMPEA, the average grain size was measured to be 9.7 ± 1.5 μm in the X-Y plane and 10.1 ± 2.7 μm in the X-Z plane. The average grain size of $Nb_{15}Ta_{10}W_{75}$ RMPEA decreases to 7.4 ± 2.7 μm in the X-Y plane and 6.1 ± 2.4 μm in the X-Z plane. It should be noted that the area measurement method was used for this purpose, which is based on the area of each grain, as following [50]:

$$d_i = 2(A_i / \pi)^{1/2} \tag{18}$$

$$d = \frac{\sum_{i=1}^{N} A_i \, d_i}{\sum_{i=1}^{N} A_i} \tag{19}$$

where A_i is the area of grain i, d_i is the equivalent diameter based on the area of grain i, d is the average grain size obtained by weighting each grain area. This method was selected due to the columnar grain morphology with irregular boundaries. It considers the overall size of the grains rather than focusing solely on the longest dimension, so this detection method was more representative.

Figs. 6(b_1–b_2) show the distribution grain misorientation angles. For NbMoTaW, the proportion of LAGBs is 38.5% in the X-Y plane and 36.4% in the X-Z plane. In $Nb_{15}Ta_{10}W_{75}$, they increase to 46.4% and 43.5%, respectively. The HAGBs (>15°) in both the RMPEAs show a uniform Gaussian distribution, without the presence of second peaks. These results demonstrate that the compositional optimization through Mo subtraction and proportional adjustment effectively increases the fraction of LAGBs and refines the grain size.

The statistics of GND are displayed in Figs. 6(c_1–c_4). The average GND values in NbMoTaW are $1.5\times10^{14}/m^2$ in the X-Y plane and $1.9\times10^{14}/m^2$ in the X-Z plane, with area fractions of dislocation density ranging from 0 to $2\times10^{14}/m^2$ at 80.0% and 70.1%, respectively. For $Nb_{15}Ta_{10}W_{75}$, the average GND values are $1.9\times10^{14}/m^2$ in the X-Y sections and $2.3\times10^{14}/m^2$ in the X-Z sections, and area fractions of dislocation density ranging from 0 to $2\times10^{14}/m^2$ are 71.2 % and 59.7 %, respectively. This result reflects that $Nb_{15}Ta_{10}W_{75}$ have the higher dislocation density than NbMoTaW in the X-Y and X-Z sections.

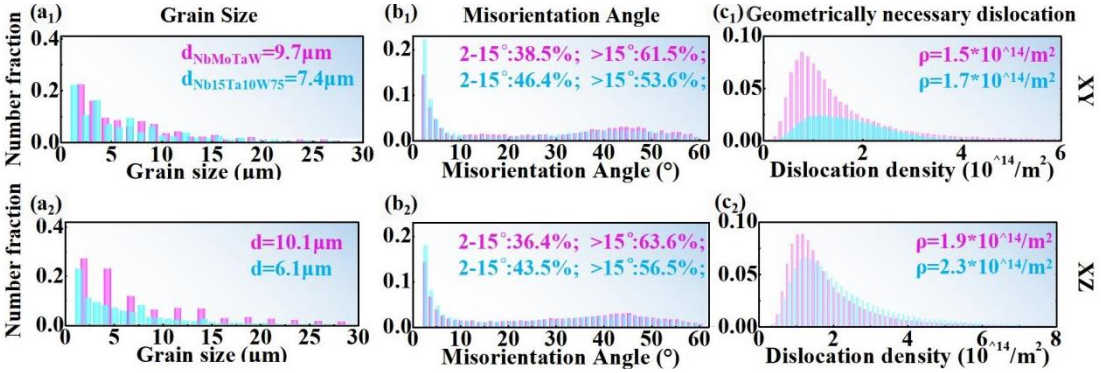

Fig. 6. EBSD analysis data: Grain size distribution (a_1–a_2); Misorientation angle (b_1–b_2) and Geometrically necessary dislocation (c_1–c_4).

To further analyze the phase type and microscopic atomic structures, bright field TEM images were taken, as shown in Figs. 7(a–b). The corresponding selected area electron diffraction (SAED) patterns of $Nb_{15}Ta_{10}W_{75}$ obtained along the $[01\text{-}1]_{BCC}$ zone axis and NbMoTaW obtained along the $[111]_{BCC}$ zone axis are shown in Figs. 7(c) and 7(d), respectively. It was observed that there were no precipitated particles in the matrix, and all the diffraction spots belong to the BCC phase. This agrees with the XRD and EBSD results. Furthermore, high-resolution TEM (HRTEM) from the low incidence axis was performed to detect possible semi-coherent precipitates, which are difficult to observe directly in the bright field TEM. The representative HRTEM results taken from matrix areas (red and orange dotted lines) are shown in Figs. 7(e–f), taken from the low-incidence axis of $[01\text{-}1]_{BCC}$ and $[001]_{BCC}$ directions, respectively. The corresponding fast Fourier transform (FFT) patterns are shown in Figs. 7 (g) and 7 (h), respectively. It was found that all the diffraction spots of NbMoTaW and $Nb_{15}Ta_{10}W_{75}$ belong to the BCC structure, without the presence of a second phase. The interplanar spacings of $[011]_{BCC}$ in $Nb_{15}Ta_{10}W_{75}$ and $[110]_{BCC}$ in NbMoTaW are about 0.214 and 0.215 nm respectively, as shown in Figs. 7(i-j). The respective lattice parameter are measured to be 3.02 Å and 3.03 Å, which are close to each other. These values are also consistent with the XRD results.

The grain boundary morphology and corresponding elemental distribution in $Nb_{15}Ta_{10}W_{75}$ are shown in Fig. 7(k). It is observed that the Nb content is relatively low at the grain boundary, and Ta and O are uniformly distributed, whereas W displays an obvious segregation. The SAED map along the $[01\text{-}1]_{BCC}$ zone axis (Fig. 7(a) and (l)) of $Nb_{15}Ta_{10}W_{75}$ RMPEA shows only the BCC structure without any second phase at the grain boundary. It is worth noting here that observing the dislocation morphology

in $Nb_{15}Ta_{10}W_{75}$ RMPEA through TEM experiment is difficult due to the challenges in sample preparation and observation, as explained in Supplementary Note 2.

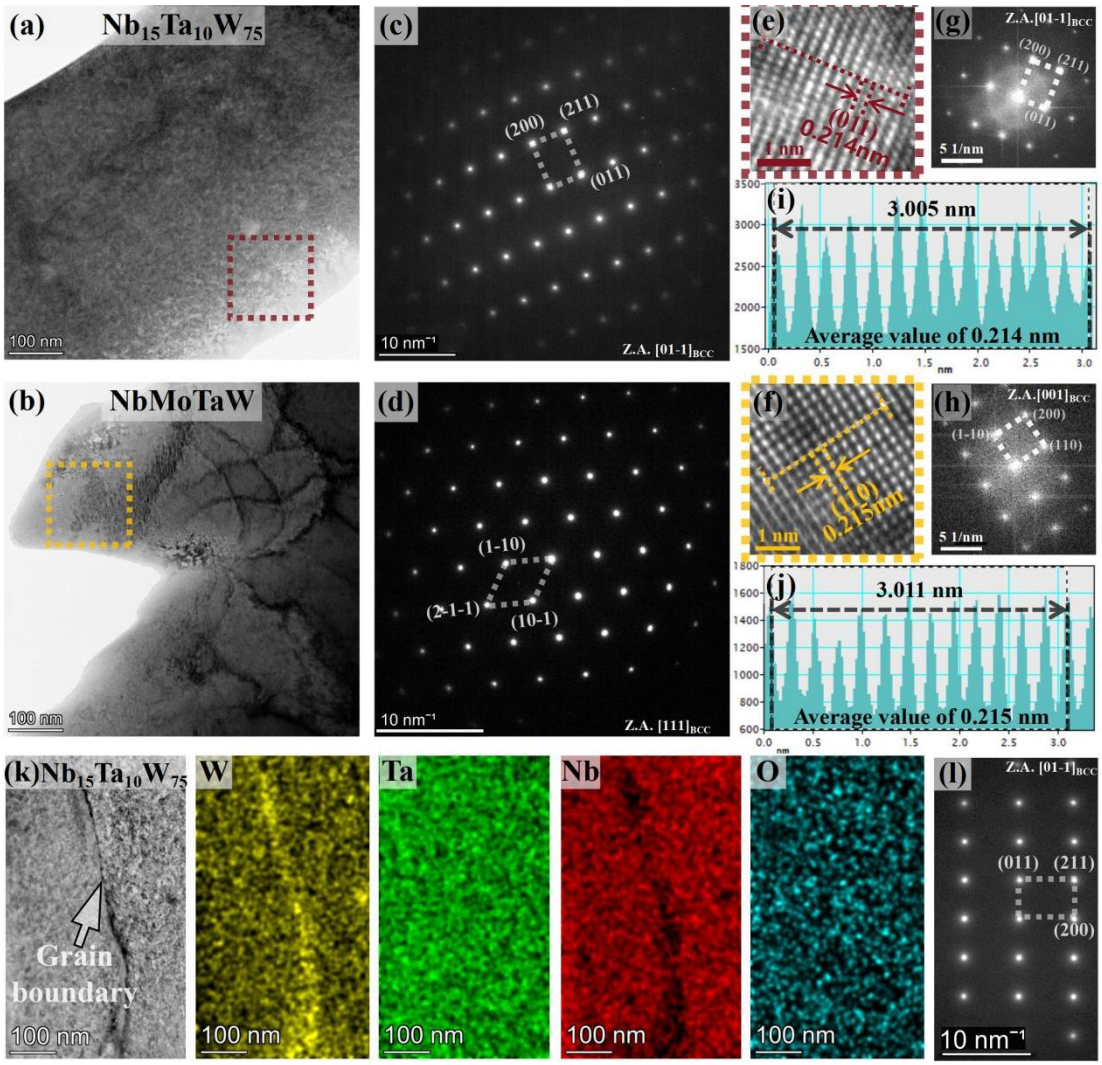

Fig. 7. TEM bright-field images of NbMoTaW and $Nb_{15}Ta_{10}W_{75}$ samples (a–b) and the corresponding selected area electron diffraction patterns (c–d); High-resolution TEM image taken from red and orange dotted region (e–f) and the corresponding fast Fourier transform patterns (g–h); Measurement of interplanar spacing for NbMoTaW and $Nb_{15}Ta_{10}W_{75}$ samples (i–j); a bright field image illustrating the grain boundary morphology in $Nb_{15}Ta_{10}W_{75}$ RMPEA and corresponding element distribution maps (k); selected area electron diffraction pattern of matrix containing the grain boundaries (l).

NbMoTaW and $Nb_{15}Ta_{10}W_{75}$ RMPEAs have similar lattice parameters mainly due to the following factors. Firstly, Nb [23], Mo [23], Ta [23], and W [23] have the similar atomic radii,143, 136, 143, and 137 pm, respectively, since they are all transition metals

and concentrated in Groups 5 and 6 of the periodic table. Adjusting the element ratio in Nb-Mo-Ta-W system alloys does not significantly alter the overall lattice parameters because the atomic radii are comparable. Secondly, both NbMoTaW and $Nb_{15}Ta_{10}W_{75}$ have only the BCC crystal structures. Distributing elements with similar sizes randomly within the same lattice structures makes it easier to obtain similar lattice parameters. Finally, NbMoTaW and $Nb_{15}Ta_{10}W_{75}$ RMPEAs have similar degrees of lattice distortion (Table1) by adjusting the element ratio in Nb-Mo-Ta-W alloy system, which are 3.1% and 2.6% respectively. This further ensures that the lattice distortion caused by the random distribution of elements has a similar effect on the lattice constant.

3.2. Mechanical properties

The engineering compressive stress-strain curves of LPBF $Nb_{15}Ta_{10}W_{75}$ reveal a significant improvement in strength and plasticity at RT, as shown in Fig. 8(a). Specifically, the compressive yield and fracture strengths increase significantly from 1103 ± 15 and 1203 ± 20 MPa in NbMoTaW to 1409 ± 10 and 1520 ± 25 MPa, respectively, in $Nb_{15}Ta_{10}W_{75}$. Plasticity also slightly increases from 3.8 ± 0.2 to 5.3 ± 0.1 %. The fractured surfaces after RT compression were observed by SEM and are shown in Fig. 8(b). The long axis of the compressed sample is parallel to the X direction (Fig. 4(f)), and the fractography is observed at their Y-Z planes. NbMoTaW displays characteristic cleavage fracture features and a relatively smooth fracture surface, whereas $Nb_{15}Ta_{10}W_{75}$ exhibits quasi-cleavage fracture characterized by short and curved quasi-cleavage steps.

The high-temperature engineering stress-strain responses of $Nb_{15}Ta_{10}W_{75}$ are shown in Fig. 8(c). The compressive yield strength at 1000, 1200, 1400, and 1600 ℃ are 1009 ± 15, 942 ± 10, 841 ± 14, and 640 ± 10 MPa, respectively. The samples deformed at 1000, 1200, and 1400 ℃ exhibit continuous hardening until failure, while a peak in stress is observed at 1600 ℃. The latter might be due to the dislocation slip transition from the cross-kinking to diffusion-controlled mechanism at ultrahigh temperatures [27]. The yield strength of $Nb_{15}Ta_{10}W_{75}$ RMPEAs at different temperatures is compared with that of NbMoTaW reported by Senkov. et al [6] in Fig. 8(d). It can be seen that the yield strength of the former is substantially higher.

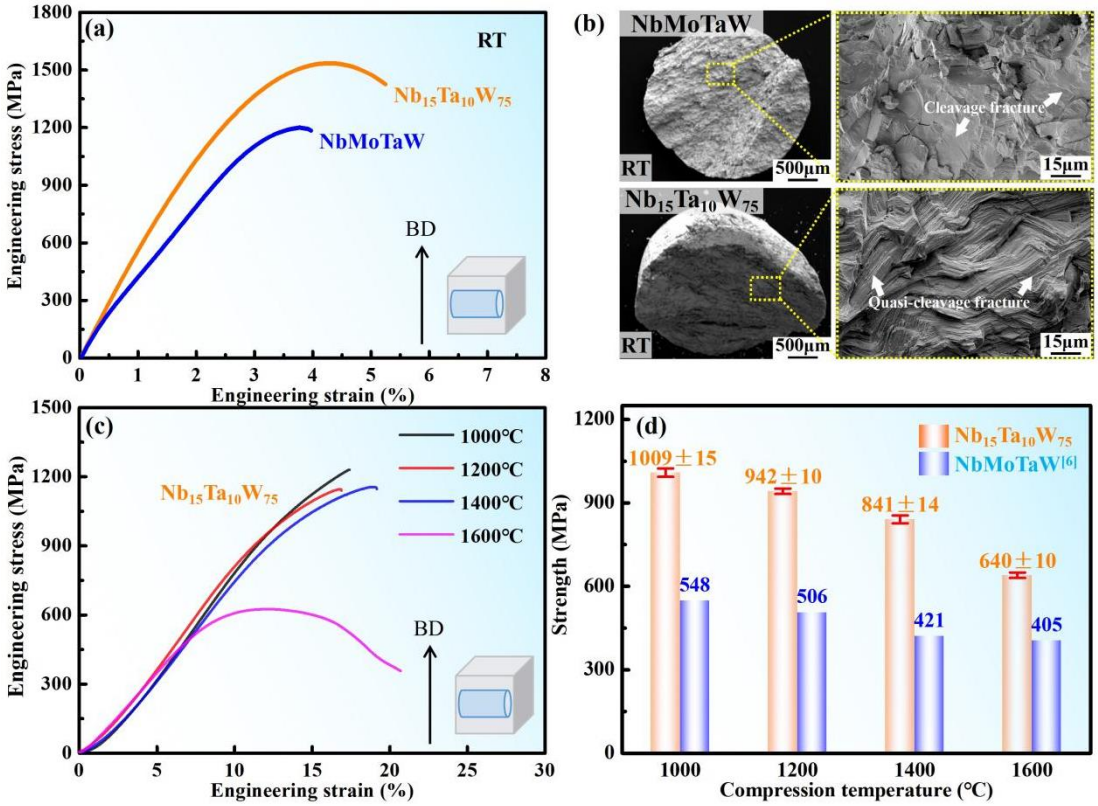

Fig. 8. Engineering compressive stress-strain curves at RT (a); Fracture morphologies at RT (b); Engineering compressive stress-strain curves at high temperature (c); Histogram of yield strength at different temperatures (d).

4. Discussion

4.1. Effect of composition optimization on printability

The defect morphologies in NbMoTaW and $Nb_{15}Ta_{10}W_{75}$ RMPEAs with different scanning speeds and laser power was characterized using OM. Furthermore, the relative densities of these samples were measured by gas expansion density tester, as shown in Fig. 9. It was observed that the dominant defects in printed samples vary with the scanning speed and laser power. Firstly, the size and quantity of pores in NbMoTaW and $Nb_{15}Ta_{10}W_{75}$ RMPEAs generally increase with the scanning speed (>400 mm/s). For example, as the scanning speed increased from 400 to 1600 mm/s, the densities of NbMoTaW and $Nb_{15}Ta_{10}W_{75}$ decrease from 92.4% and 98.4% to 65.2% and 83.5%, respectively, at a fixed laser power of 200 W. This is due to the insufficient energy density at higher speeds, which fails to fully melt the high melting point powders, leading to the formation of the lack of fusion pores [47]. Secondly, cracks become the predominant defects in NbMoTaW and $Nb_{15}Ta_{10}W_{75}$,at the scanning speeds below 400 mm/s. For instance, at a fixed scan speed of 200 mm/s, the cracks in NbMoTaW and

$Nb_{15}Ta_{10}W_{75}$ gradually expand and run through the samples as the laser power increased from 200 to 400 W. Meanwhi, while the densities of NbMoTaW and $Nb_{15}Ta_{10}W_{75}$ decrease from 81.4% and 97.3% to 75.4% and 88.5%, respectively. This is because the higher power inputs result in excess energy, which, in turn, leads to the accumulation of the thermal stresses beyond material's strength and, ultimately, resulting in cracks [47]. In summary, inadequate energy input results in pore formation, whereas excessive energy input results in crack formation.

Furthermore, based on the results of relative density measurements and observations on the defects, the porosity level and cracking tendency of $Nb_{15}Ta_{10}W_{75}$ are significantly reduced compared to those of NbMoTaW at the same laser power and scanning speed. This can be attributed to the combination of powder and thermodynamic characteristics. In $Nb_{15}Ta_{10}W_{75}$, a higher content of W powders with better laser absorption enhances the melting of powders (Fig. 4(d)), which results in a better ability to fill pores and cracks. Apart from the influence of powder, the broader *LR* and lower *LV* of $Nb_{15}Ta_{10}W_{75}$ also contribute to better fluidity of the molten liquid for filling the shrinkage pores and cracks that might have formed during solidification, resulting in superior density than NbMoTaW printed samples (Table 1). Moreover, the smaller *VC* and μ/B values of $Nb_{15}Ta_{10}W_{75}$ are also beneficial for improving crack resistance, which reduce the thermal-induced deformation levels and enhance the matrix toughness to resist cracking (Table 1). The red boxes in Fig. 9 mark the optimal process parameters for $Nb_{15}Ta_{10}W_{75}$ and NbMoTaW, suggesting a wider window for the former than that for NbMoTaW, which is also manifests as a higher density and superior printability in the former.

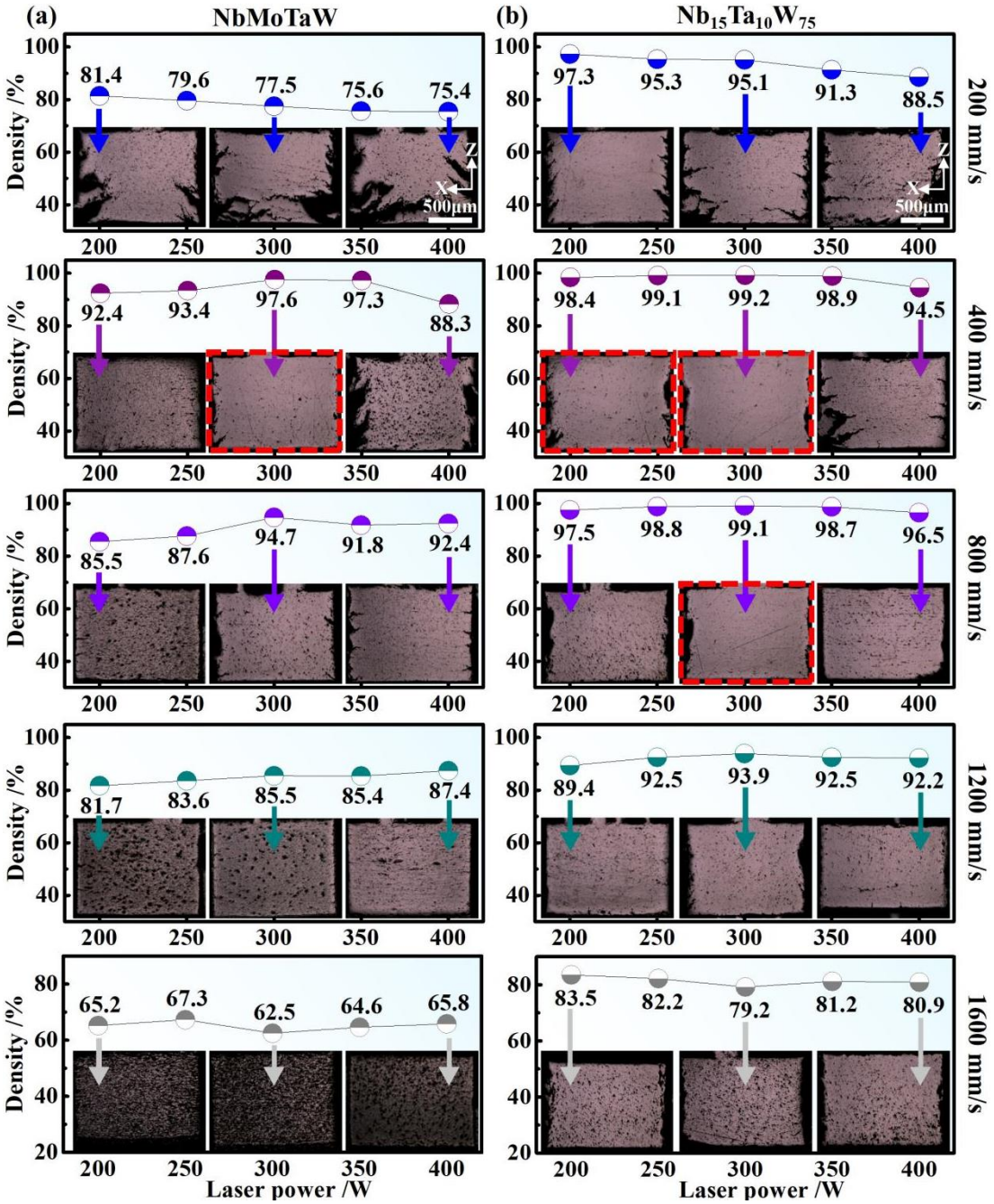

Fig. 9. Optical micrographs showing the defect morphologies in the LPBF NbMoTaW (a) and $Nb_{15}Ta_{10}W_{75}$ (b) samples fabricated with different scanning speeds and laser powers.

4.2. Effect of composition optimization on microstructure

It is well known that the nucleation and growth of grains during solidification significantly affect the microstructural characteristics [51]. However, using the equilibrium phase diagram to analyze the non-equilibrium solidification path caused by LPBF process is inappropriate, as it does not involve dynamic calculations. Therefore,

the Gulliver-Scheil model in the Thermo-calc software was used to calculate the non-equilibrium solidification paths at the cooling rate of 10^7 Ks^{-1}, as shown in Fig. 10(a). This model assumes that elements completely diffuse in the liquid, but do not diffuse in solids, which is consistent with the fast solidification characteristics of the LPBF process [18,19]. It was observed that the solidification sequence in both the alloys is Liquid to BCC. The solidification temperature ranges for $Nb_{15}Ta_{10}W_{75}$ and NbMoTaW are 3000 to 3230 ℃ and 2600 to 2840 ℃, respectively. $Nb_{15}Ta_{10}W_{75}$ can completely solidify within the temperature range of 3000 to 3230 ℃, while NbMoTaW would still be in the liquid state in that range. This is because $Nb_{15}Ta_{10}W_{75}$ contains a large content of high melting point W element (Fig. 10(b)) than NbMoTaW (Fig. 10(c)).

The influence of the compositional optimization on the grain nucleation is analyzed based on the non-equilibrium solidification path. The kinetic undercooling ($\Delta T_{k,}$) significantly affects grain nucleation during LPBF, and can be estimated using the following equations [52]:

$$\Delta T_K = \frac{v_s}{\eta} \tag{20}$$

$$v_s = v\cos\varphi \tag{21}$$

$$\eta = \frac{\Delta H_f \mathrm{v}_0}{\mathrm{K}_\beta T_L^2} \tag{22}$$

where v_s denotes the growth velocity at the grain tip, η is the interfacial kinetic coefficient, v is the laser scanning speed (mm/s), φ is the included angle (°) between the directions of v and v_s, ΔH_f is the formation enthalpy (kJ/mol), v_0 is the sound velocity (m/s), k_β is the Boltzmann constant, and T_L is the liquid temperature (℃). The $\Delta T_{k,}$ values are controlled by T_L and ΔH_f. The liquid-to-solid transition temperature of $Nb_{15}Ta_{10}W_{75}$ exceed that of NbMoTaW by about 400 ℃, due higher T_L value of it. ΔH_f for different pairs of Nb, Mo, Ta, and W, and NbMoTaW and $Nb_{15}Ta_{10}W_{75}$ are shown in Fig. 10(d). $Nb_{15}Ta_{10}W_{75}$ has lower ΔH_f than NbMoTaW due to the higher W content in it. Moreover, W has the lowest formation enthalpy with Nb and Ta in the Nb-Mo-Ta-W system. The combination of higher T_L and lower ΔH_f in $Nb_{15}Ta_{10}W_{75}$ RMPEA can lead to a lower η, which is beneficial to obtain a larger ΔT_k than that of NbMoTaW. A higher ΔT_k can increase the nucleation rate [28], resulting in finer grains in $Nb_{15}Ta_{10}W_{75}$. Apart from the influence of ΔH_f on the grain size, the higher content of high melting point W in $Nb_{15}Ta_{10}W_{75}$ can preferentially nucleate and provide abundant

nucleation sites during the solidification process, which is also benefits the formation of finer grains. Furthermore, $Nb_{15}Ta_{10}W_{75}$ has a lower Gibbs free energy (ΔG) than NbMoTaW (estimated using the Thermo-calc software), as shown in Fig. 10(e). ΔG exerts a significant impact on nucleation [53]. A lower ΔG indicates that $Nb_{15}Ta_{10}W_{75}$ is more favorable for homogeneous nucleation, which results in finer grain size.

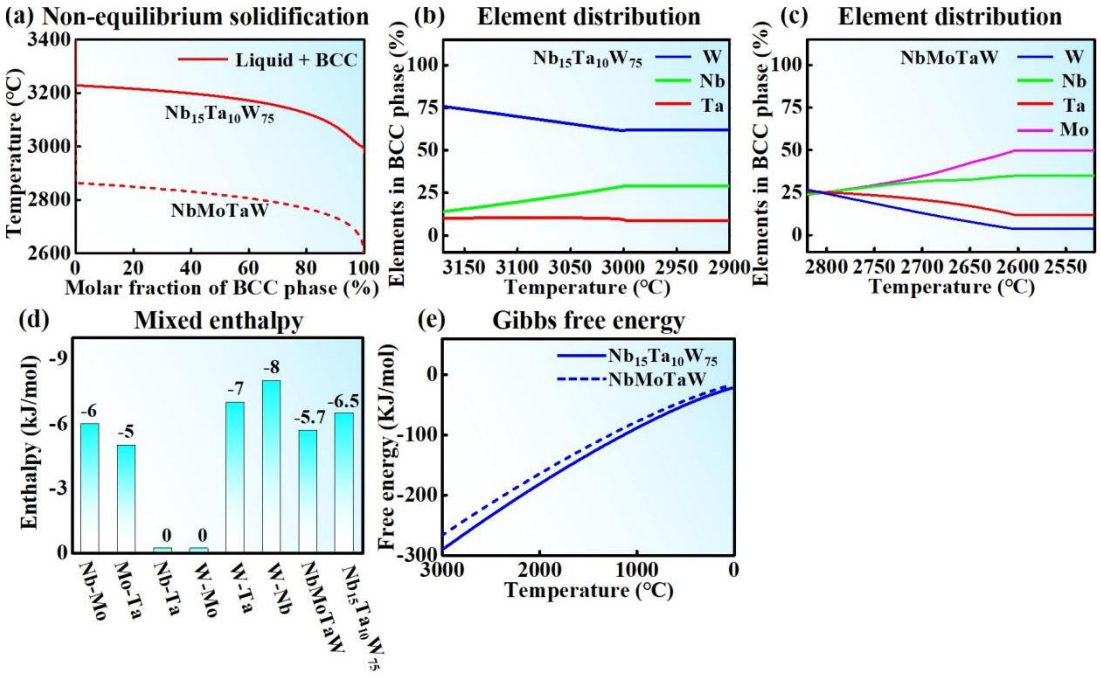

Fig. 10. Thermodynamic parameters related to nucleation: Non-equilibrium solidification path using the Thermo-calc software (a); Element distribution in the BCC Phase for NbMoTaW (b) and $Nb_{15}Ta_{10}W_{75}$ (c); Formation enthalpies (d), Gibbs free energy (e).

The rapid cooling rate inherent to the LPBF process restricts atomic diffusion during solidification and makes the solute elements accumulate at the grain boundaries, particularly thosewith slower diffusion rates. The accumulated solute elements can restrict the grain growth, resulting in grain refinement. Therefore, it is crucial to analyze the impact of element optimization on grain growth by examining the elemental distribution at the grain boundaries of $Nb_{15}Ta_{10}W_{75}$, which was accomplished through APT. The two-dimensional (2D) reconstruction compositional maps, displayed in Fig. 11(a), show that Nb and Ta are slightly depleted (Figs. 11(b_1-b_3)), W is uniformly distributed (Fig. 11(b_3)), O is significantly enriched at the grain boundaries (Figs. 11(b_4)). On this basis, the grain boundaries are revealed by constructing the surface with equal concentration O content of 5.4 at.%, as shown in Fig. 11(c). Oxygen in the

Nb-Mo-Ta-W alloys is prone to segregate to the grain boundaries, which assists the identification of grain boundaries [54]. To quantitatively analyze the distribution of elements at the grain boundaries, a one-dimensional (1D) composition diagram perpendicular to the equal concentration surface of O was constructed in Fig. 11(d) at the location marked in Fig. 11(c). The concentrations of Nb and Ta at the grain boundary are low (about 0.09% and 3.7%), whereas their respective values in the grain interiors (about 11.9% and 16.5%, respectively) are very close to the matrix composition (about 15.0% and 10.0%, respectively), further confirming our identifications of grain boundaries and interior in Fig. 11(c). In contrast, the concentration of O at the grain boundaries reaches to about 5.1%, which is higher than that in the grain interior, or ~0.17%. It is worth noting that the concentration of W at the grain boundary (90.5%) is significantly higher than that inside the grain (66.7%), implying the segregation of W to the grain boundary. For a better illustration of the distribution of W at the grain boundary, a 2D concentration map is created, confirming a higher concentration of W at the grain boundary compared to the matrix, as shown in Fig. 11 (e_1–e_2).

The segregation of W to the grain boundaries significantly affects grain growth during solidification. To compare the influence of diffusion rates of Nb, Mo, Ta, and W on the grain growth, their diffusion coefficients were calculated using the relation [14]:

$$\varsigma = \varsigma_0 \exp\left(\frac{-Q_D}{RT}\right) \quad \textbf{(23)}$$

where ς_0 is the intrinsic diffusion coefficient (m^2/s), and Q_D is the activation energy of diffusion (kJ/mol). The temperature-dependence of diffusion coefficients of Nb, Mo, Ta, and W, estimated using Eq. (23), is presented in Fig. 11(f), and the corresponding parameters are listed in Table 2 [14]. The values of ς_0 and Q_D were obtained through experiments on binary or ternary refractory metals which consist of Nb, Mo, Ta, or W and without other metallic elements [14]. These binary or ternary refractory alloys contain the same elements as NbMoTaW and $Nb_{15}Ta_{10}W_{75}$ RMPEAs, thus the ς_0 and Q_D of them are used for approximation. Besides, ς_0 and Q_D do not have the significant correlation, both of which were derived based on the experiments [14]. It was found that the diffusion coefficients decrease with decreasing temperature, and W exhibits the fastest downward trend than Nb, Ta, and Mo. Secondly, the diffusion rates in the liquid

phase in $Nb_{15}Ta_{10}W_{75}$ and NbMoTaW were calculated based on the non-equilibrium solidification path, and the diffusion rates of each element in the liquid phase were separated, as shown in Fig. 11(g). The diffusion rate of the liquid phase and constituent elements (Nb, Ta, and W) in $Nb_{15}Ta_{10}W_{75}$ are lower than that of NbMoTaW. This is because $Nb_{15}Ta_{10}W_{75}$ contains a large amount of W with a low diffusion coefficient, which slows down the diffusion rate in the liquid phase. This, in turn, limits the grain growth by impeding the movement of the solidification front. Another factor that makes grain growth unfavorable in $Nb_{15}Ta_{10}W_{75}$ is that the supercooled liquid containing segregated solute atoms will accumulate at the grain boundaries during solidification. The undercooled liquid contains a high content of W element, which has been confirmed by non-equilibrium solidification path (Fig. 10(b); > 61%) and APT results (Fig. 11(d); > 64%). In comparison, the W content in the undercooled liquid of NbMoTaW is relatively low of about 25% through non-equilibrium solidification path calculation in Fig. 10(c).

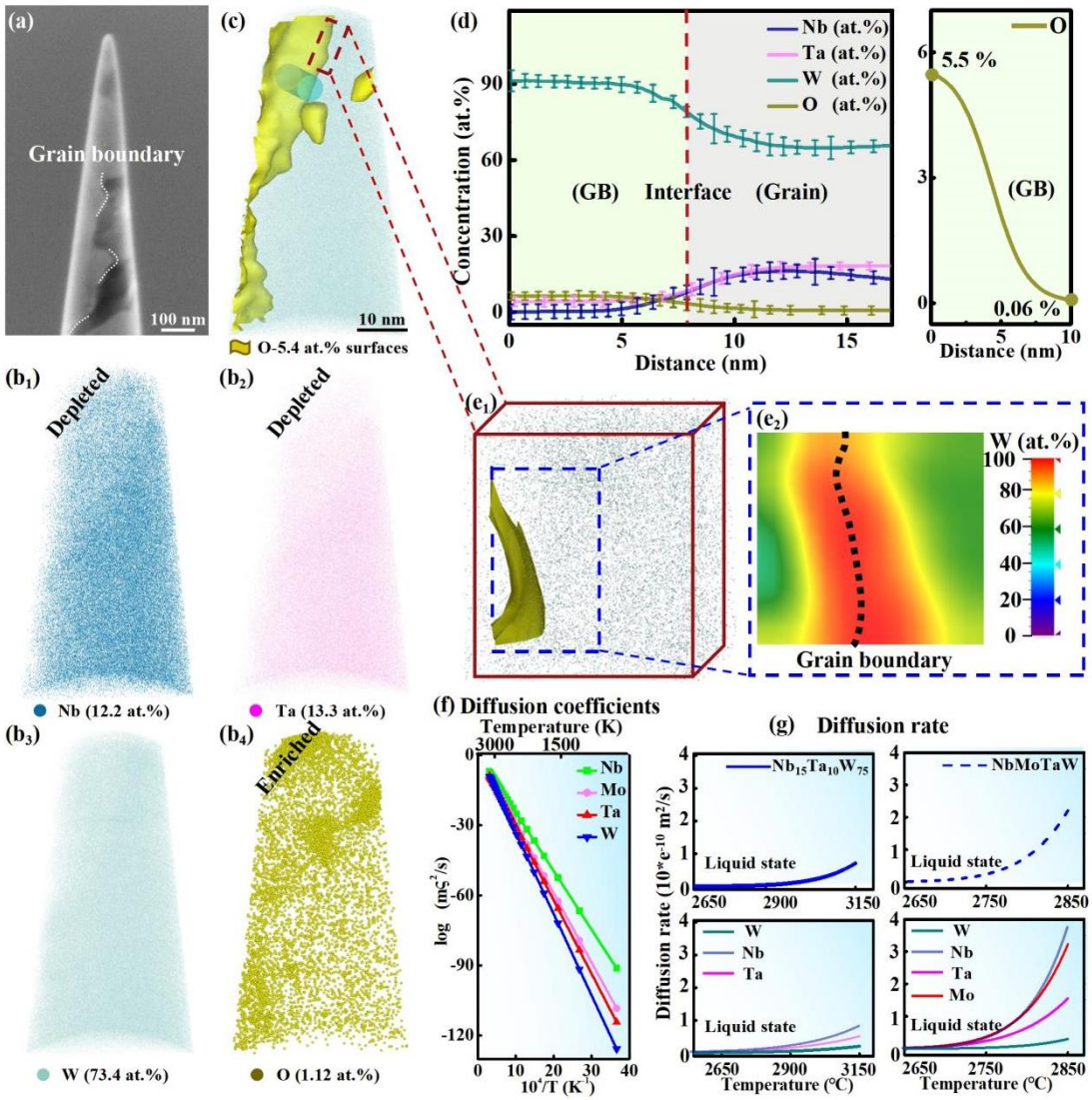

Fig. 11. Local elemental distribution near the grain boundaries for $Nb_{15}Ta_{10}W_{75}$: SEM image of 3D-APT specimens containing the grain boundaries (a); 2D reconstruction atom maps obtained by APT test reflects the distribution of Nb, Ta, W and O near the grain boundaries (b_1–b_4); 3D reconstruction of grain boundaries with the equal concentration O content of 5.4 at.% (c); 1D concentration diagram perpendicular to the equal concentration surface of O reflects the distribution of elements at the grain boundaries (d); The enlarged map of local grain boundaries obtained from the 3D reconstruction (e_1) and the corresponding 2D concentration projection of W near the grain boundaries (e_2); Thermodynamic analysis related to grain growth: Temperature-dependent diffusion coefficients (f); The diffusion rate of liquid and corresponding constituent elements for $Nb_{15}Ta_{10}W_{75}$ and NbMoTaW RMPEAs at different temperatures (g).

Table 2. Intrinsic diffusion coefficients and activation energies of diffusion.

	Nb	Mo	Ta	W	
ς_0 (10^{-4} m^2/s)	4.5	1.45	6.2	46	[14]
Q_D (KJ/mol)	480.2	567.3	601.7	666.2	[14]

Schematic diagrams depicting grain nucleation and growth based on the non-equilibrium solidification map (Fig. 10(a)) are shown in Figs. 12(a–b) to elucidate the effects of compositional optimization on the microstructural development. At the first temperature range T_1, $Nb_{15}Ta_{10}W_{75}$ exhibits a rapid formation of BCC solid phase, until reaching a peak molar phase fraction of 100%, whereas NbMoTaW remains in the liquid phase. The larger degree of ΔT_k, higher melting point and smaller values of ΔG in $Nb_{15}Ta_{10}W_{75}$ facilitate the preferential grain nucleation in it. At T_2, NbMoTaW begins transforming into BCC solid phase, exhibiting a maximum transformation rate of ~100%. While $Nb_{15}Ta_{10}W_{75}$ has completely transformed into a solid phase at the previous temperature stage. NbMoTaW exhibits a smaller undercooling in this temperature range, leading to a coarser grain size in it than in $Nb_{15}Ta_{10}W_{75}$. By T_3 stage, the liquid phase completely transforms into the BCC solid phase in both the alloys. Grain growth is difficult due to the rapid cooling rate during LPBF and the sluggish diffusion in RMPEAs due to lattice distortion. It is further restricted in $Nb_{15}Ta_{10}W_{75}$ due to the high content of W with slow diffusion rate segregating at grain boundaries and hindering the movement of the solidification front. Therefore, $Nb_{15}Ta_{10}W_{75}$ optimized from Nb-Mo-Ta-W system has a finer grain size, as confirmed by the experiment in Figs. 12(c–d).

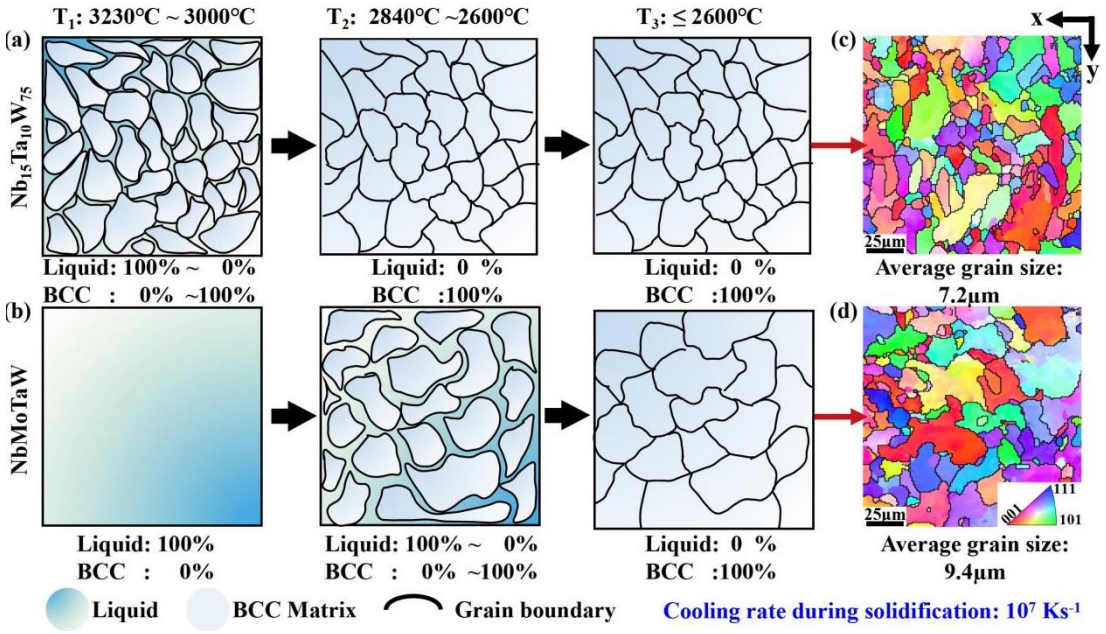

Fig. 12. Schematic representation of nucleation and grain growth illustrating the regulatory mechanism of composition optimization (a-b); Grain size statistics derived from EBSD providing confirmation of the optimized composition (c-d).

4.3. Effect of composition optimization on the mechanical properties

The crystalline defects within the microstructure, such as dislocations, grain and twin boundaries, second phases, and precipitates contribute to the strength of an alloy [55]. For NbMoTaW and $Nb_{15}Ta_{10}W_{75}$ strengthening from precipitates, twins, or second phases are ruled out as they were not found in the microstructure. Therefore, the main contributors are solid solution, grain boundary, and dislocation strengthening mechanisms [56]. Their contributions can be approximately quantified with the following relations [57, 58]:

$$\sigma_y = \sigma_0 + \Delta\sigma_S + \Delta\sigma_{GB} + \Delta\sigma_{Dis} \quad (24)$$

$$\sigma_0 = \sum x_i \sigma_i \quad (25)$$

$$\Delta\sigma_{GB} = \mathrm{K}d^{-1/2} \quad (26)$$

$$\Delta\sigma_{Dis} = \mathrm{M}\alpha\mu b\rho^{1/2} \quad (27)$$

where σ_y is the total compressive yield strength, σ_0 is the lattice friction stress (which is estimated by combining the frictional stresses of pure metal using the rule of mixtures [59-62]), $\Delta\sigma_{GB}$ is grain boundary strengthening contribution [60], k is the Hall-Petch slope (~210 MPa·μm$^{1/2}$ for refractory metals [60]), d is the average grain size (measured from the EBSD data in X-Y plane in Figs. 6(a_1-a_2)), $\Delta\sigma_s$ is solid solution strengthening

contribution (calculated based on the Toda-Caraballo model given in section 2.1), $\Delta\sigma_{Dis}$ is dislocation strengthening contribution (estimated by using the Bailey-Hirsch equation in Eq. (27) [60], M is Taylor factor (~2.733 for BCC refractory metals [60]), α is an empirical constant (~0.5 for BCC metals [60]), and ρ is the dislocation density (estimated from the XRD analysis (Fig. 4(e)).

The contributions of different strengthening mechanisms and their proportions are shown in Fig. 13. It is seen that σ_0 contributes the most of the strength in $Nb_{15}Ta_{10}W_{75}$, while $\Delta\sigma_s$ is the most contributor of strength for NbMoTaW. $Nb_{15}Ta_{10}W_{75}$ with higher content of W has a higher σ_0 than NbMoTaW, which is since W has a large lattice friction stress value (550 MPa) than Nb (240 MPa), Mo (433 MPa), and Ta (189 MPa) [62]. Amongst the strengthening mechanisms, the contribution of SSH is the most (354 and 337 MPa for NbMoTaW and $Nb_{15}Ta_{10}W_{75}$, respectively) accounting for 32.8% and 25.4% of the total strengths, respectively. SSH in RMPEAs is attributed to the severe lattice distortion which hinders dislocation movement, where μ and the atomic mismatch play pivotal roles [61-64]. μ is calculated by Eq. (3), and atomic mismatch was reflected by *XDX*' in section 2.1. $Nb_{15}Ta_{10}W_{75}$ has a higher μ compared to NbMoTaW, along with a lower *XDX'* (Table 1). Their combination leads to a similar SSH in both the alloys. The enhanced strength in $Nb_{15}Ta_{10}W_{75}$ (compared to NbMoTaW) mainly comes from the contributions of the grain boundary and dislocation strengthening mechanisms, which are 58 and 118 MPa, respectively, as it possesses a smaller grain size (Figs. 6(a_1-a_2)) and higher dislocation density (Fig. 4(e)).

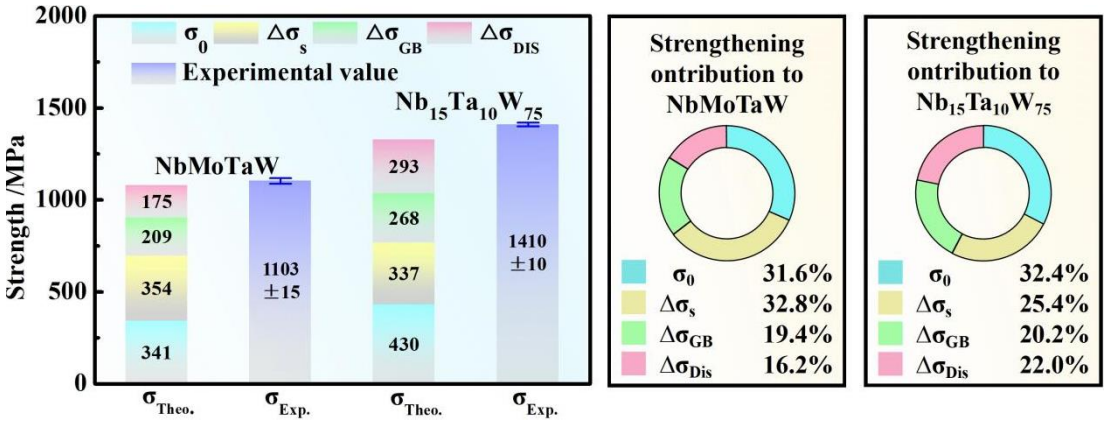

Fig. 13. Estimated contributions (and corresponding proportions) of various strengthening mechanisms.

4.4. High-temperature strength

The work hardening rate curves of $Nb_{15}Ta_{10}W_{75}$ RMPEA at different temperatures were plotted to analyze high-temperature deformation behavior, as shown in Fig. 14(a). The work hardening behavior for $Nb_{15}Ta_{10}W_{75}$ at different temperatures can be approximately partitioned into two stages. In stage I, the work-hardening rates decrease precipitously [65], whereas they decrease relatively slowly in stage II and shows a continuous strain hardening behavior [65], for as temperatures below 1400 ℃, Indicating a strong resistance to deformation. The work hardening behavior of $Nb_{15}Ta_{10}W_{75}$ exhibits a significant transition when the temperature exceeds 1400 ℃. A continuous strain hardening behavior is observed when the true strain exceeds 10% (Stage II),indicating that dislocation slip occurs readily

The glide of screw dislocations dominates the high-temperature strength and deformation behavior of conventional BCC metals and alloys [66]. The high-temperature deformation of RMPEAs, in contrast, undergoes a transition from a screw to edge dislocation dominant one [29]. The strength associated with each of these mechanisms can be estimated using the following equations [67, 68]:

$$\sigma_{Screw}\left(\dot{\varepsilon},T\right)=2.74\left(\tau_{xk}\left(\dot{\varepsilon},T\right)+\tau_{k}\left(\dot{\varepsilon},T\right)\right) \tag{28}$$

$$\tau_{xk}\left(\dot{\varepsilon},T\right)=\frac{\pi E_{v/i}}{ab0.5}\left[1-\left(\frac{\Delta H}{E_{v/i}}\right)^{2/3}\right] \tag{29}$$

$$\tau_{k}\left(\dot{\varepsilon},T\right)=\tau_{b}+\tau_{c}\left[3.26\left(\frac{\Delta H}{\Delta E_{p}}-0.06\frac{E_{k}}{\Delta E_{p}}+1.07\sqrt{10}\right)^{-1}-1.58\frac{\Delta E_{p}}{E_{k}}\right] \tag{30}$$

$$\Delta H=KTln\left(\dot{\varepsilon}_{0}/\dot{\varepsilon}\right) \tag{31}$$

$$\sigma_{Edge}\left(\dot{\varepsilon},T\right)=3.06\tau_{yo}\exp\left[-\frac{1}{0.55}\left(\frac{KT}{\Delta E_{b}\ln\left(\dot{\varepsilon}_{0}/\dot{\varepsilon}\right)}\right)^{0.91}\right] \tag{32}$$

$$\tau_{y0}=0.040\Psi^{-1/3}\overline{G}\left(\frac{1+\overline{\nu}}{1-\overline{\nu}}\right)^{4/3}\left[\frac{\sum_{n}c_{n}\Delta V_{n}^{2}}{b^{6}}\right]^{2/3} \tag{33}$$

$$\Delta E_{b}=2.00\Psi^{1/3}\overline{G}b^{3}\left(\frac{1+\overline{\nu}}{1-\overline{\nu}}\right)^{2/3}\left[\frac{\sum_{n}c_{n}\Delta V_{n}^{2}}{b^{6}}\right]^{1/3} \tag{34}$$

$$\Delta V_{n}=100\sqrt{\sum_{i=1}^{n}c_{i}\left(1-\frac{V_{i}}{\sum_{i=1}^{n}c_{i}V_{i}}\right)^{2}} \tag{35}$$

In the above, σ_{Screw} and σ_{Edge} are the stresses required for the glide of a screw or edge dislocation, respectively, $\dot{\varepsilon}$ is the strain rate of 0.0025 mm/s as mentioned in section 2.4, τ_{xk} is the stress to break the cross-kink of a screw dislocation, ΔH is the enthalpy that is a function of $\dot{\varepsilon}$ and temperature, and E_v, E_i and E_k are the vacancy

formation energy, self-interstitial formation energy, and average kink formation energy, respectively. (These values are obtained by weighing the values of different single elements, and the specific values are listed in Table 3.) τ_k is the stress that causes the dislocation kink to slide across the energy barrier, τ_b is similar to back stress. τ_c is a characteristic stress, ΔE_p is the concentrated-weighted average of the elemental properties estimated from first principles (which for $Nb_{15}Ta_{10}W_{75}$ and NbMoTaW are ~60 and 320 meV, respectively [68, 69]). $\dot{\varepsilon}_0$ is a reference strain rate of $10^4 s^{-1}$ [68]. Ψ is the line tension coefficient (=1/6). υ is the Burger vector constant. ΔV_n is the misfit volume of atom. c_i, V_i are the atomic fractions and atom volume of the i-th elements respectively. Note that the model for screw dislocation glide has only one fitting parameter, while the edge dislocation one is an elasticity-based, parameter-free model. It should be noted that the parameters for screw dislocation are difficult to calculate accurately at present, and the edge dislocation is predicted based on the empirical parameters [67]. Thus, the models for screw and edge dislocations can only be used for approximate estimation of the lower and upper limits of strength, respectively.

The estimated variations in the strength for $Nb_{15}Ta_{10}W_{75}$ are displayed in Fig. 14(b) along with the experimentally measured values. It is observed that the strength curve predicted by the screw dislocation model decreases more rapidly with increasing temperature, than that predicted by the edge dislocation model. The strength values of $Nb_{15}Ta_{10}W_{75}$ and NbMoTaW RMPEAs are within the intersection range of the predicted curves for the screw and edge dislocations, demonstrating a transition in strength from screw to edge dislocations with the temperature. The plastic deformation behavior dominated by the screw dislocations typically exhibits continuous work hardening, while the deformation dominated by edge dislocations exhibits a rapid decrease in work hardening [68]. Specifically, $Nb_{15}Ta_{10}W_{75}$ shows a transition from continuous hardening deformation to a rapid decrease in hardening rate with increasing temperature, as shown in Fig. 14(a). This observation also supports the hypothesis of a transition of dominant deformation from screw to edge dislocations as temperature increases.

The temperature range over which plastic deformation transitions from being the screw to edge dislocation dominant one is usually defined as the softening temperature ($T_c = 0.3–0.5T_m$), which is significantly influenced by alloy's melting point [69-71]. Within the temperature range of T_c, there is no significant decrease in high temperature strength and a strength plateau appears. This is due to the equal mobility for both types of dislocations over the transition range, which contributes to high-temperature strength

retention [29]. Therefore, delaying the appearance of T_c range is an effective strategy to maintain high-temperature strength, which can be realized by enhancing the melting point of the material. Specifically, the estimated plateau strength for $Nb_{15}Ta_{10}W_{75}$ is approximately 920 MPa and occurs from 1000 to 1400 ℃, which is much larger than that measured for NbMoTaW (480 MPa) over the same temperature range, as shown in Fig. 14(b). $Nb_{15}Ta_{10}W_{75}$ has higher T_c (~950–1550 ℃) than NbMoTaW (~840–1400 ℃) according to the phase diagram in Fig. 10(a), which confirms the effective retention of the screw-to-edge transition on high-temperature strength due to the high melting point. In addition, severe lattice distortion hinders dislocation migration at high temperatures and enhances strength [28].

Fig. 14(c) compares high-temperature compressive properties of $Nb_{15}Ta_{10}W_{75}$ and previously reported materials [10, 13, 72-77]. It can be found that the compressive strength of $Nb_{15}Ta_{10}W_{75}$ above 1200℃ is notably superior to all the previously reported RMPEAs. The compressive strengths between 1000 and 1200℃ are only inferior to those of $W_{0.5}(TaTiVCr)_{0.5}$, $Nb_2MoWC_{0.96}$, and $NbTaW_{0.5}(Mo_2C)_{0.2}$. To analyze the difference in high-temperature strength between $Nb_{15}Ta_{10}W_{75}$ and previously reported RMPEAs, their maximum softening temperature ($T_{m0.5}$) and atomic mismatch degree (δ_r) are compared, as shown in Fig. 14(d). The value of δ_r effectively reflects the degree of lattice mismatch for RMPEA. The resistance to dislocation movement and the effect of solid solution strengthening increase with the value of δ_r, which can be estimated using the following formula [62]:

$$\delta_r = 100\sqrt{\sum_{i=1}^{n} c_i\left(1-\frac{r_i}{\sum_{i=1}^{n} c_i r_i}\right)^2} \tag{36}$$

where c_i, r_i are the atomic fractions and atom radii of the i-th element, respectively. The calculated values of δ_r are shown in Fig. 14(d). It reveals that $Nb_{15}Ta_{10}W_{75}$ s exhibits a slightly smaller lattice mismatch (2.8 %) compared to NbMoTaW (3.3 %), which is consistent with *XDX'* results (Table 1). It was observed that the atomic mismatch degree of $Nb_{15}Ta_{10}W_{75}$ is lower than those reported for other RMPEAs. This is due to the significant size differences between various elements (such as Ti, Zr, Hf or C) in the reported ones, compared to $Nb_{15}Ta_{10}W_{75}$. In addition, $T_{m0.5}$ of $Nb_{15}Ta_{10}W_{75}$ is about 1550 ℃, while it is below 1400 ℃ for $W_{0.5}(TaTiVCr)_{0.5}$, $Nb_2MoWC_{0.96}$, and $NbTaW_{0.5}(Mo_2C)_{0.2}$.Thus, the testing temperature of 1400 ℃ represents the transition temperature for $Nb_{15}Ta_{10}W_{75}$, while it exceeds those of $W_{0.5}(TaTiVCr)_{0.5}$, $Nb_2MoWC_{0.96}$, and $NbTaW_{0.5}(Mo_2C)_{0.2}$ Therefore, $W_{0.5}(TaTiVCr)_{0.5}$, $Nb_2MoWC_{0.96}$, and

$NbTaW_{0.5}(Mo_2C)_{0.2}$ can exhibit higher strength below $T_{m0.5}$ due to the higher degree of δ_r in them, although $Nb_{15}Ta_{10}W_{75}$ has excellent high temperature strength compared to other reported RMPEAs.

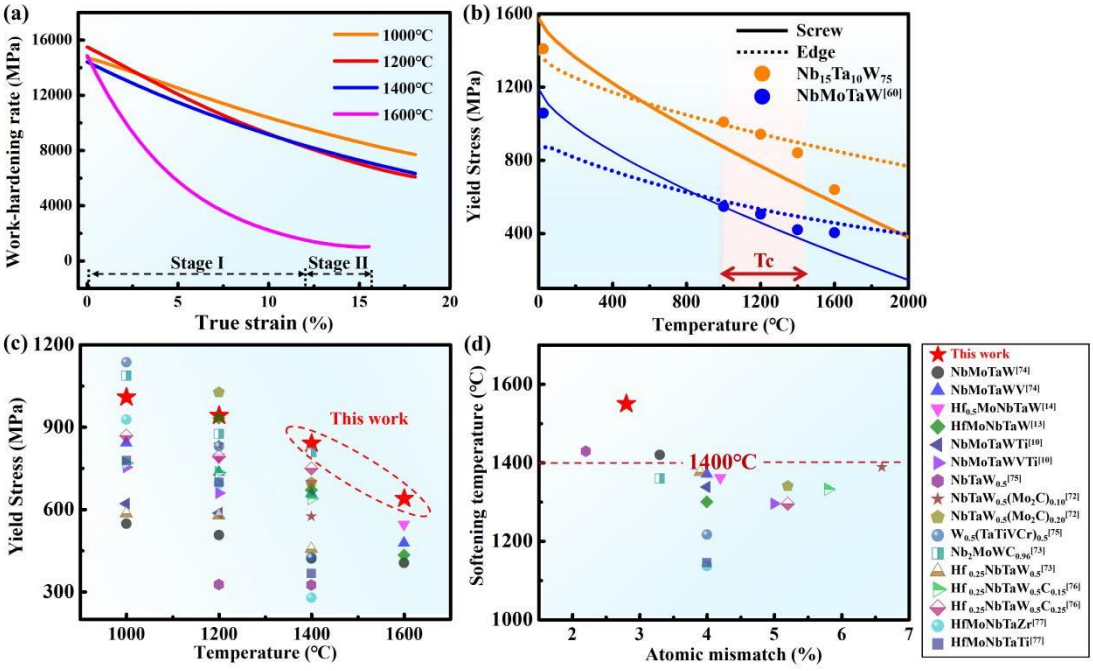

Fig. 14. Work hardening rate curves for $Nb_{15}Ta_{10}W_{75}$ RMPEA at different temperatures (a); High-temperature compressive properties and predicted curves for edge and screw dislocation strengthening mechanism (b); High-temperature compressive strength comparison with reported RMPEAs (c); Comparison of softening temperature and atomic mismatch with reported RMPEAs (d).

Table 3. Vacancy, self-interstitial and average kink formation energies of the single element.

	Nb	Mo	Ta	W	
E_v (meV)	2850	2900	2950	3800	[68]
E_i (meV)	5253	7417	5832	9548	[68]
E_k (meV)	640	500	585	901	[68]

5. Conclusions

In this study, a composition optimization strategy was proposed for identifying the optimum composition in the Nb-Mo-Ta-W RMPEA system to retain high-temperature strength and enhance printability simultaneously, and $Nb_{15}Ta_{10}W_{75}$ RMPEA is identified and fabricated using LPBF. The following are some conclusions that can be drawn from this study:

1. An increase in the number of different elements in the alloy enhances SSH, which is crucial for retaining strength at high temperatures, but deteriorates the printability in the Nb-Mo-Ta-W alloy system. By using the multiplication plot of SSH and thermodynamic calculations, $Nb_{15}Ta_{10}W_{75}$ was determined to be the optimal chemical composition for the best strength and printability synergy.

2. The superior printability of $Nb_{15}Ta_{10}W_{75}$ is attributed to its higher laser absorption rate, broader liquid range, and smaller liquid viscosity, which collectively reduce the tendency for pore and crack formation and result in a broader printing process window. The density of LPBF $Nb_{15}Ta_{10}W_{75}$ is 99.2%, higher than that of NbMoTaW with 97.6%.

3. By analyzing the influence of thermodynamic properties on the grain nucleation and growth in $Nb_{15}Ta_{10}W_{75}$, it was found that the composition optimization design with high W content significantly enhances the nucleation rates and retards the grain growth rate, leading to a refined average grain size of ~6.1 ± 1.2 μm.

4. $Nb_{15}Ta_{10}W_{75}$ RMPEA shows superior yield strength of 1457 MPa at RT, which can be attributed mainly to the dislocation and grain boundary strengthening mechanisms. Additionally, a ultrahigh-temperature strength of 640 MPa at 1600 ℃ was obtained, which is attributed to its high melting point and the severe lattice distortion introduced in it through the composition optimization.

Declaration of Competing Interest

The authors declare that they do not have any commercial or associative interest that could have appeared to influence the work reported in this paper.

Acknowledgement

This work was financially supported by National Key R&D Program of China (No. 2022YFB4602102). We would like to acknowledge the supports from Instrumental Analysis Center of Shanghai Jiao Tong University and Instrument and equipment sharing platform of School of Materials Science and Engineering, SJTU. YZ would like to thank the support by A*STAR via the Advanced Models for Additive Manufacturing (AM2) programme (No. M22L2b0111).

References

[1] R. Feng, B. Feng, M.C. Gao, C. Zhang, J.C. Neuefeind, J.D. Poplawsky, Y. Ren, K. An, M. Widom, P.K. Liaw, Superior High-Temperature Strength in a Supersaturated Refractory High-Entropy Alloy, Adv Mater 33(48) (2021) 2102401.

[2] X.J. Hua, P. Hu, H.R. Xing, J.Y. Han, S.W. Ge, S.L. Li, C.J. He, K.S. Wang, C.J. Cui, Development and Property Tuning of Refractory High-Entropy Alloys: A Review, Acta metall sin-Engl 35(8) (2022) 1231-1265.

[3] S. Chen, C. Qi, J. Liu, J. Zhang, Y. Wu, Recent Advances in W-Containing Refractory High-Entropy Alloys-An Overview, Entropy 24(11) (2022) 1553.

[4] B. Gorr, M. Azim, H.J. Christ, T. Mueller, D. Schliephake, M. Heilmaier, Phase equilibria, microstructure, and high temperature oxidation resistance of novel refractory high-entropy alloys, J alloy compd 624 (2015) 270-278.

[5] O.N. Senkov, D.B. Miracle, K.J. Chaput, J.P. Couzinie, Development and exploration of refractory high entropy alloys—A review, J Mater res 33(19) (2018) 3092-3128.

[6] O.N. Senkov, G.B. Wilks, D.B. Miracle, C.P. Chuang, P.K. Liaw, Refractory high-entropy alloys, Intermetallics 18(9) (2010) 1758-1765.

[7] C.Y. Yap, C.K. Chua, Z.L. Dong, Z.H. Liu, D.Q. Zhang, L.E. Loh, S.L. Sing, Review of selective laser melting: Materials and applications, Appl Phys Rev 2(4) (2015) 041101.

[8] D. Wang, L. Liu, G. Deng, C. Deng, Y. Bai, Y. Yang, W. Wu, J. Chen, Y. Liu, Y. Wang, X. Lin, C. Han, Recent progress on Additive manufacturing of multi-material structures with laser powder bed fusion, Virtual Phys Prototy 17(2) (2022) 329-365.

[9] H. Zhang, Y. Zhao, S. Huang, S. Zhu, F. Wang, D. Li, Manufacturing and Analysis of High-Performance Refractory High-Entropy Alloy via Selective Laser Melting (SLM), Materials 12(5) (2019) 720.

[10] Z.D. Han, N. Chen, S.F. Zhao, L.W. Fan, G.N. Yang, Y. Shao, K.F. Yao, Effect of Ti additions on mechanical properties of NbMoTaW and VNbMoTaW refractory high entropy alloys, Intermetallics 84 (2017) 153-157.

[11] T. Li, W. Jiao, J. Miao, Y. Lu, E. Guo, T. Wang, T. Li, P.K. Liaw, A novel ZrNbMoTaW refractory high-entropy alloy with in-situ forming heterogeneous structure, Mat Sci Eng: A 827 (2021) 142061.

[12] Y. Tong, L. Bai, X. Liang, Y. Chen, Z. Zhang, J. Liu, Y. Li, Y. Hu, Influence of alloying elements on mechanical and electronic properties of NbMoTaWX (X = Cr, Zr, V, Hf and Re) refractory high entropy alloys, Intermetallics 126 (2020) 106928.

[13] Y.X. Wan, Study on the Preparation and Mechanical Properties of Rare Metals Nb/Mo/Ta/W Based Ultra-high-temperature High-entropy Alloys, China University of Mining and Technology (2021)
[14] G. Neumann, C. Tuijn, Self-diffusion and impurity diffusion in pure metals: handbook of experimental data, Elsevier 2011.
[15] H. Zhang, Y. Zhao, J. Cai, S. Ji, J. Geng, X. Sun, D. Li, High-strength NbMoTaX refractory high-entropy alloy with low stacking fault energy eutectic phase via laser, Mater Design 201 (2021) 109462.
[16] Z. Sun, Y. Ma, D. Ponge, S. Zaefferer, E.A. Jägle, B. Gault, A.D. Rollett, D. Raabe, Thermodynamics-guided alloy and process design for dditive manufacturing, Nat Commun 13(1) (2022) 4361.
[17] X. Jintao, Q. Meng, D. Shangzhe, P. Kumar, Z. Jie, J. Yubo, Y. Zhenyu, X. Yong, D. Peng, F. Kai, L. Zhuguo, Z. Qingjun, L. Xiubing, U. Ramamurty, Enhancing the strength and plasticity of laser powder bed fused NbMoTaW refractory high-entropy alloy via Ti alloying, J Alloy Compd 31 (2024) 175043.
[18] C. Panwisawas, Y. Gong, Y.T. Tang, R.C. Reed, J. Shinjo, Additive manufacturability of superalloys: Process-induced porosity, cooling rate and metal vapour, Addit Manuf 47 (2021) 102339.
[19] J. Zhang, J. Gao, B. Song, L. Zhang, C. Han, C. Cai, K. Zhou, Y. Shi, A novel crack-free Ti-modified Al-Cu-Mg alloy designed for selective laser melting, Addit Manuf 38 (2021) 101829.
[20] Z. Jin, Z. Zhang, K. Demir, G.X. Gu, Machine Learning for Advanced Additive manufacturing, Matter 3(5) (2020) 1541-1556.
[21] D. Tomus, P.A. Rometsch, M. Heilmaier, X. Wu, Effect of minor alloying elements on crack-formation characteristics of Hastelloy-X manufactured by selective laser melting, Addit Manuf 16 (2017) 65-72.
[22] Y.X. Wan, Study on the Preparation and Mechanical Properties of Rare Metals Nb/Mo/Ta/W Based Ultra-high-temperature High-entropy Alloys, China University of Mining and Technology (2021).
[23] T.K. Kai, H. Hsuan, W.W. Ren, Y.J. Wei, T.C. Wei, Edge-dislocation-induced ultrahigh elevated temperature strength of HfMoNbTaW refractory high-entropy alloys, Sci Technol Adv Mat 23(1) (2022) 642-654.
[24] S. Yin, Y. Zuo, A. A. Odeh, H. Zheng, X.G. Li, J. Ding, S.P. Ong, M. Asta, R.O. Ritchie, Atomistic simulations of dislocation mobility in refractory high-entropy

alloys and the effect of chemical short-range order, Nat Commun 12(1) (2021) 4873.
[25] R. Duan, X. Jintao, Z. Yakai, Z. Qingjun, Y. Zhenyu, X. Yong, D. Peng, X. Lifang, F. kai, L. Zhuguo, L. Xiubing, U. Ramamurty, High entropy alloys amenable for laser powder bed fusion: a thermodynamics guided machine learning search, Addit Manuf 11 (2024) 104195.
[26] A. Roy, P. Sreeramagiri, T. Babuska, B. Krick, P.K. Ray, G. Balasubramanian, Lattice distortion as an estimator of solid solution strengthening in high-entropy alloys, Mater Charact 172 (2021) 110877.
[27] F.L.Wang, G.H. Balbus, S.Z.Xu, Y.Q.Su, J.Shin, P.F. Rottmann4, Multiplicity of dislocation pathways in a refractory multiprincipal element alloy, Science 370 (2020) 95-101.
[28] Q. Li, H. Zhang, D. Li, Z. Chen, F. Wang, M. Wu, Comparative study of the microstructures and mechanical properties of laser metal deposited and vacuum arc melted refractory NbMoTa medium-entropy alloy, Int J Refract Met H 88 (2020) 105195.
[29] Y. Tong, L. Bai, X. Liang, M. Hua, J. Liu, Y. Li, J. Zhang, Y. Hu, Mechanical performance of $(NbTaW)_{1-x}Mo_x$ (x = 0, 0.05, 0.15, 0.25) refractory high entropy alloys: Perspective from experiments and first principles calculations, J alloy compd 873 (2021) 159740.
[30] L. Wenyang, H. Yufeng, W. Yao, L. Wensheng, M. Yunzhu, W-a-Nb solid solutions prepared by vacuum arc melting: Microstructure evolution and mechanical properties, Vacuum 212 (2023) 4873.
[31] E.P. George, W.A. Curtin, C.C. Tasan, High entropy alloys: A focused review of mechanical properties and deformation mechanisms, Acta Mater 188 (2020) 435-474.
[32] I. Toda-Caraballo, A general formulation for solid solution hardening effect in multicomponent alloys, Scripta Mater 127 (2017) 113-117.
[33] Z. An, S. Mao, Y. Liu, L. Wang, H. Zhou, B. Gan, Z. Zhang, X. Han, A novel HfNbTaTiV high-entropy alloy of superior mechanical properties designed on the principle of maximum lattice distortion, J Mater Sci Technol 79 (2021) 109-117.
[34] Y. Chen, Y. Fang, X. Fu, Y. Lu, S. Chen, H. Bei, Q. Yu, Origin of strong solid solution strengthening in the CrCoNi-W medium entropy alloy, J Mater Sci Technol 73 (2021) 101-107.
[35] W.S. Choi, B.C. Cooman, S. Sandlöbes, D. Raabe, Size and orientation effects in

partial dislocation-mediated deformation of twinning induced plasticity steel micro pillars, Acta Mater 98 (2015) 391-404.
[36] R.L. Fleischer, Substitutional solution hardening, Acta Mater 11 (1963).
[37] T. Caraballo, P.E.J. Rivera-Díaz-del-Castillo, Modelling solid solution hardening in high entropy alloys, Acta Mater 85 (2015) 14-23.
[38] N. Ali, L. Zhang, D. Liu, H. Zhou, K. Sanaullah, C. Zhang, J. Chu, Y. Nian, J. Cheng, Strengthening mechanisms in high entropy alloys: A review, Mater Today Commun 33 (2022) 104686.
[39] D. Duoyang, C. Bing, L. Suzhi, D. Xiangdong, S. Jun, Effect of local lattice distortion on the core structure of edge dislocation in NbMoTaW multi-principal element alloys and the subsystems, Mat Sci Eng: A 855 (2022) 143869.
[40] S. Wang, D. Li, J. Xiong, Prediction of elastic properties of face-centered cubic high-entropy alloys by machine learning, T Nonferr Metal Soc, 33 (2023) 518-530.
[41] X. Wang, Y. Wang, X. Wang, Modeling of thickness effect on the creep properties of Ni-based superalloys, Multidiscip Model Ma 13(3) (2017) 464-470.
[42] Z. Fan, P. Tsakiropoulos, A. P. Miodownik, A generalized law of mixtures, J Mater Sci, 29 (1994) 141-150.
[43] K. Sindo, A criterion for cracking during solidification, Acta Mater 88 (2015) 366-374.
[44] J.Y. He, H. Wang, H.L. Huang, X.D. Xu, M.W. Chen, Y. Wu, X.J. Liu, T.G. Nieh, K. An, Z.P. Lu, A precipitation-hardened high-entropy alloy with outstanding tensile properties, Acta Mater 102 (2016) 187-196.
[45] Y.H. Zhao, X.Z. Liao, Z. Jin, R.Z. Valiev, Y.T. Zhu, Microstructures and mechanical properties of ultrafine grained 7075 Al alloy processed by ECAP and their evolutions during annealing, Acta Mater 52(15) (2004) 4589-4599.
[46] H.W. Deng, M.M. Wang, Z.M. Xie, T. Zhang, X.P. Wang, Q.F. Fang, Y. Xiong, Enhancement of strength and ductility in non-equiatomic CoCrNi medium-entropy alloy at room temperature via transformation-induced plasticity, Mat Sci Eng: A 804 (2021) 140516.
[47] P. Gu, T. Qi, L. Chen, T. Ge, X. Ren, Manufacturing and analysis of VNbMoTaW refractory high-entropy alloy fabricated by selective laser melting, Int J Refract Met H 105 (2022) 105834.
[48] N.T. Tayade, M.P. Tirpude, Frustrated microstructures composite PbS material's size perspective from XRD by variant models of Williamson–Hall plot method, Bull.

Mater. Sci 46(20) (2023) 102843.
[49] M. Calcagnotto, D. Ponge, E. Demir, D. Raabe, Orientation gradients and geometrically necessary dislocations in ultrafine grained dual-phase steels studied by 2D and 3D EBSD, Mat Sci Eng: A 527(10-11) (2010) 2738-2746.
[50] Y.A. Coutinho, S.C.K. Rooney, E.J. Payton, Analysis of ebsd grain size measurements using microstructure simulations and a customizable pattern matching library for grain perimeter estimation, Metall Mater trans A 48(5) (2017) 2375-2395.
[51] S. Luo, Y. Su, Z. Wang, Microstructural evolution and mechanisms in additively manufactured AlCrCuFeNix complex concentrated alloys via selective laser melting, J alloy compd 870 (2021) 159443.
[52] D. Wang, C. Song, Y. Yang, Y. Bai, Investigation of crystal growth mechanism during selective laser melting and mechanical property characterization of 316L stainless steel parts, Mater Design 100 (2016) 291-299.
[53] D. Huang, J. Yan, X. Zuo, Co-precipitation kinetics, microstructural evolution and interfacial segregation in multicomponent nano-precipitated steels, Mater Charact 155 (2019) 109786.
[54] Z. Wang, H. Wu, Y. Wu, H. Huang, X. Zhu, Y. Zhang, H. Zhu, X. Yuan, Q. Chen, S. Wang, X. Liu, H. Wang, S. Jiang, M.J. Kim, Z. Lu, Solving oxygen embrittlement of refractory high-entropy alloy via grain boundary engineering, Materials Today 54 (2022) 83-89.
[55] H. Huang, J. Wang, H. Yang, S. Ji, H. Yu, Z. Liu, Strengthening CoCrNi medium-entropy alloy by tuning lattice defects, Scripta Mater 188 (2020) 216-221.
[56] X. Liu, M. Zhang, Y. Ma, W. Dong, R. Li, Y. Lu, Y. Zhang, P. Yu, Y. Gao, G. Li, Achieving ultrahigh strength in CoCrNi-based medium-entropy alloys with synergistic strengthening effect, Mat Sci Eng: A 776 (2020) 139028.
[57] J.M. Park, E.S. Kim, H. Kwon, P. Sathiyamoorthi, K.T. Kim, J.H. Yu, H.S. Kim, Effect of heat treatment on microstructural heterogeneity and mechanical properties of 1%C-CoCrFeMnNi alloy fabricated by selective laser melting, Addit Manuf 47 (2021) 102283.
[58] X.H. Du, W.P. Li, H.T. Chang, T. Yang, G.S. Duan, B.L. Wu, J.C. Huang, F.R. Chen, C.T. Liu, W.S. Chuang, Y. Lu, M.L. Sui, E.W. Huang, Dual heterogeneous structures lead to ultrahigh strength and uniform ductility in a Co-Cr-Ni medium-entropy alloy, Nat Commun 11(1) (2020) 2390.

[59] W. Huang, X. Wang, J. Qiao, Y. Wu, Microstructures and mechanical properties of TiZrHfNbTaWx refractory high entropy alloys, J alloy compd 914 (2022).
[60] X.F. Xie, Z.M. Xie, R. Liu, Q.F. Fang, C.S. Liu, W.Z. Han, X. Wu, Hierarchical microstructures enabled excellent low-temperature strength-ductility synergy in bulk pure tungsten, Acta Mater 228 (2022) 165187.
[61] Y. Chen, Z. Xu, M. Wang, Y. Li, C. Wu, Y. Yang, A single-phase V0.5Nb0.5ZrTi refractory high-entropy alloy with outstanding tensile properties, Mat Sci Eng: A 792 (2020) 139774.
[62] Q. Li, H. Zhang, D. Li, Z. Chen, Z. Qi, The effect of configurational entropy on mechanical properties of single BCC structural refractory high-entropy alloys systems, Int J Refract Met H 93 (2020) 105370.
[63] C. Yin, D. Terentyev, T. Zhang, S. Nogami, S. Antusch, C.C. Chang, R.H. Petrov, T. Pardoen, Ductile to brittle transition temperature of advanced tungsten alloys for nuclear fusion applications deduced by miniaturized three-point bending tests, Int J Refract Met H 95 (2021) 105464.
[64] Y. Wan, X. Wang, Z. Zhang, J. Mo, B. Shen, X. Liang, Structures and properties of the (NbMoTaW)100−xCx high-entropy composites, J alloy compd 889 (2021) 161645.
[65] C. Xiang, C. Han, M. Siming, Insights into flow stress and work hardening behaviors of a precipitation hardening AlMgScZr alloy: Experiments and modeling, Int J Plasticity 172 (2024) 103852.
[66] X.R. Zhou, X.Y. Wang, L. Fey, S.C. He, I. Beyerlein, P.H. Cao, J. Marian, Models of dislocation glide and strengthening mechanisms in bcc complex concentrated alloys, MRS Bulletin 12 (2023) 1111-1118.
[67] I.H. Kim, H.S. Oh, K.S. Lee, E.S. Park, Optimization of conflicting properties via engineering compositional complexity in refractory high entropy alloys, Scripta Mater 199 (2021) 113839.
[68] C. Baruffi, F. Maresca, W.A. Curtin, Screw vs. edge dislocation strengthening in body-centered-cubic high entropy alloys and implications for guided alloy design, MRS Communications 12(6) (2022) 1111-1118.
[69] S. He, X. Zhou, D. Mordehai, J. Marian, Thermal super-jogs control the high-temperature strength plateau in Nb-Mo-Ta-W alloys, Acta Mater 244 (2023) 118539.
[70] W. Huang, J. Hou, X. Wang, J. Qiao, Y. Wu, Excellent room-temperature tensile ductility in as-cast Ti37V15Nb22Hf23W3 refractory high entropy alloys,

Intermetallics 151 (2022) 107735.
[71] Y. Wan, J. Mo, X. Wang, Z. Zhang, B. Shen, X. Liang, Mechanical Properties and Phase Stability of WTaMoNbTi Refractory High-Entropy Alloy at Elevated Temperatures, Acta metall sin-Engl 34(11) (2021) 1585-1590.
[72] S. Wu, D. Qiao, H. Zhao, J. Wang, Y. Lu, A novel NbTaW0.5 (Mo2C)x refractory high-entropy alloy with excellent mechanical properties, J alloy compd 889 (2021) 161800.
[73] Y. Zhang, Q. Wei, P. Xie, X. Xu, An ultrastrong niobium alloy enabled by refractory carbide and eutectic structure, Mater Res Lett 11(3) (2022) 169-178.
[74] J.P. Couzinie, O.N. Senkov, D.B. Miracle, G. Dirras, Comprehensive data compilation on the mechanical properties of refractory high-entropy alloys, Data Brief 21 (2018) 1622-1641.
[75] S. Alvi, O.A. Waseem, F. Akhtar, High Temperature Performance of Spark Plasma Sintered W0.5(TaTiVCr)0.5 Alloy, Metals 10(11) (2020) 1512.
[76] S. Wu, D. Qiao, H. Zhang, J. Miao, H. Zhao, J. Wang, Y. Lu, T. Wang, T. Li, Microstructure and mechanical properties of C Hf0.25NbTaW0.5 refractory high-entropy alloys at room and high temperatures, J Mater Sci Technol 97 (2022) 229-238.
[77] K.K. Tseng, C.C. Juan, S. Tso, H.C. Chen, C.W. Tsai, J.W. Yeh, Effects of Mo, Nb, Ta, Ti, and Zr on Mechanical Properties of Equiatomic Hf-Mo-Nb-Ta-Ti-Zr Alloys, Entropy 21(1) (2018) 15.